Contribution of Crevasse Advection and Mixed Mode Calving to Glacier Dynamics

by

Brandon Berg

A dissertation submitted in partial fulfillment
of the requirements for the degree of
Doctor of Philosophy
(Physics)
in The University of Michigan
2021

Doctoral Committee:

Associate Professor Jeremy Bassis, Co-Chair
Associate Professor Robert Deegan, Co-Chair
Professor Charles Doering (Deceased)
Associate Professor Gretchen Keppel-Aleks
Associate Professor Kevin Wood

Brandon Berg
brberg@umich.edu

ORCID iD: 0000-0002-2760-6112

To all my teachers, past, present, and future, who communicate the beauty of the universe.

ACKNOWLEDGEMENTS

First and foremost, I would like to thank my wife, Kate, for her unwavering, unconditional, and unbelievable support during these past six years. None of this is possible without you. Thank you to my parents Rich and Jo-Ann for your love and support through all that I do and for encouraging me to be thoughtful, curious, and kind. To my brother Erik for being an inspiration to me from a young age and expecting the highest levels of achievement. And to my most influential teacher, Mark Bautista, without whom I may never have studied physics in the first place.

Thank you to my advisor, Jeremy, for being a fantastic mentor and advisor. I have learned so much from you over the past few years, arriving confused from the Physics department and leaving slightly less confused (but significantly happier) as a glaciologist. You consistently remind me why all of your students and mentees (myself included) have countless positive things to say. You are an extremely talented scientist and more importantly, a kind and humble person.

This dissertation would not be possible without the support of my committee: my co-chair Robert Deegan, Gretchen Keppel-Aleks, Kevin Wood, and especially Charles Doering, may he rest in peace. I also owe a great deal to my fellow vintage glaciology group members (current and emeritus): Yue Ma, Lizz Ultee, Morgan Whitcomb, Ray Watkins, Sam Kachuck, and Mac Cathles. I don't take lightly your emotional support, great advice, and putting up with my incessant sarcasm.

As I prepare for life after grad school, I am deeply grateful to Washtenaw Com-

munity College, Danette Bull, Robert Hagood, and Suzanne Albach for giving me the opportunity to find my passion for teaching. Thank you to Lauren Woolsey, Bob Cebelak, Tari Mattox, and all others at Grand Rapids Community College for your kindness as I finish this dissertation and I look forward to working with you soon.

Lastly, to Stephen DiIorio, Michael Viray, Callum Jones, Rachel Hyneman, Steve Novakov, and everyone else who has made this journey with me. I wish you all the best of luck and I will always treasure all the memories we've made together in our little corner of the universe.

TABLE OF CONTENTS

LIST OF FIGURES

Figure

LIST OF TABLES

Table

ABSTRACT

Modeling of the climate system including, but not limited to, atmospheric dynamics, ocean dynamics, and ice dynamics, is one of the crucial scientific problems of the 21st century. This work focuses on modeling of iceberg calving, the process by which high stresses within ice cause fractures and eventual detachment of icebergs from glaciers. Iceberg calving causes approximately half of mass loss of the world's glaciers, but remains poorly understood and implemented in climate models. Existing model implementations of calving exist at a wide range of spatial and temporal scales, ranging from models that seek to resolve crevasse propagation on the scale of seconds or minutes to broad parameterizations of calving implemented in ice sheet scale climate models. In this work, we seek to develop an intermediate model that can run for year to decade timescales and determines calving based on the internal stresses within the ice. We first focus on crevasse advection, the memory of previously formed crevasses within the ice and their impact on calving behavior. Second, we implement the possibility for mixed mode calving, where ice can fail either via high tensile stresses, high shear stresses, or a combination of the two. Lastly, we include submarine melt to see the combined effect of melt and mixed mode calving on glacier stability. This model is developed using the highly flexible Python finite element library FEniCS and LEoPart, a particle tracking library developed for use with FEniCS. Our novel use of particles to track previously crevassed ice provides a computationally efficient method to track glacier parameters that does not diffuse

over time. In initial model development, we identified a key numerical consideration related to the buoyant boundary condition on ice that can create unphysical results if not careful managed in a calving model. Once this issue was documented and addressed through a simple addition to the glacier momentum balance, including crevasse advection in the model, which should increase calving rates, reduces overall rate of glacier advance but is incapable of causing retreat in most cases. This indicates that other mass loss mechanisms, such as shear calving and submarine melt, are crucial to mass balance and should be included in future models whenever possible. When mixed-mode calving is included, we find that glacier behavior is highly unstable with regards to the shear strength of ice. Sharp transitions exists at shear strengths where the ice transitions from slow advance or retreat to rapid, catastrophic collapse. Including submarine melt causes further steady mass loss, but does not significantly alter the shear strength threshold necessary for rapid collapse. This shows that if models seek to model potential catastrophic glacier collapse, which is a point of current scientific contention, mixed mode failure including shear localization should be a key focus of modeling efforts.

CHAPTER I

Introduction

1.1 Motivation

Human-caused global climate change, caused primarily by the increase in carbon dioxide emissions from the accelerated burning of fossil fuels, is one of the greatest challenges faced by humanity in the upcoming century. According to Pörtner and others (2019), under the "worst-case" Representative Concentration Pathway (RCP) 8.5 scenario which assumes fossil fuel emissions continues to rise over the next next century, average global temperature is expected to rise approximately 4 degrees Celsius. The conservative RCP 2.6 scenario which requires zero carbon dioxide emissions by 2100 would result in a temperature increase of 1 degree Celsius.

These rising temperatures can cause ice, located primarily near the poles in ice sheets, to melt and raise global sea level. Two major ice sheets, massive regions of ice that cover large portions of the Earth's surface, exist in the world today. The Greenland ice sheet is the smaller of the two, and represents 6 meters of sea level rise should it completely disintegrate. The Antarctic ice sheet is significantly larger and holds enough ice to rise the world's oceans by 60 meters. Glaciers are the "flowing" portions of these ice sheets that drain the ice from the center of the ice sheets into the surrounding oceans.

Although sea-level rise is nonuniform due to ocean circulation, gravitational changes from mass redistribution, and vertical rebound by the Earth's crust and mantle, average sea-level rise over the next 100 years in the conservative Intergovernmental Panel on Climate Change (IPCC) RCP 2.5 scenario is modeled to be approximately half a meter (Pörtner and others, 2019). It is expected that even a sea-level rise under 1 meter could have a variety of negative effects upon the world's population, including more frequent extreme weather events (Zanocco and others, 2018; Bellprat and others, 2019), damaging agricultural production (Moore and others, 2017), increasing the spread of infectious diseases (Lafferty, 2009; Altizer and others, 2013), and displacing coastal populations (Hauer and others, 2016; Chen and Mueller, 2018; Barnard and others, 2019). Many effects are most likely to affect regions of the developing world, where resources to mitigate risk to sea level rise may be limited (Dasgupta and others, 2009).

While even conservative estimates could be devastating for many communities, the uncertainty in this prediction is extremely high (Pörtner and others, 2019). Particularly on the lower end of estimated sea level rise values, high uncertainties represent a large difference in necessary adaptation on the local scale. Plans for local adaptation are typically made on yearly or decadal timescales and plan for more fine-grained changes in predictions (Barnett and others, 2014; Haasnoot and others, 2020). Thus, reducing the uncertainty of sea level rise predictions over decade to century timescales is crucial for informing efforts to mitigation damage to communities at risk.

When modeling future sea level rise, approximately 50% of the mass lost from the Greenland and Antarctic ice sheets is due to iceberg calving (Depoorter and others, 2013; Khan and others, 2015). Iceberg calving is the process by which high internal stress causes brittle fractures in ice, causing icebergs to detach and discharge into the

ocean. Because iceberg calving is poorly understood and there is no widely accepted model on the best way to model calving, this process accounts for an extremely large source of uncertainty in sea level rise projections (Stocker and others, 2013; Pörtner and others, 2019; Pattyn and Morlighem, 2020). Better understanding of this process is crucial for improving overall projections of sea level rises in decade to century timescales. The focus of this work is to model the physical processes underlying the calving process to better inform future large scale climate models.

1.2 Ice as a solid and a fluid

Ice is a fascinating material that, in modeling ice dynamics on the glacier or ice sheet scale, may be thought of both as a brittle solid susceptible to rapid fracture or as a non-Newtonian fluid that deforms and flows slowly over time. At sufficiently high stresses (in the hundreds of kilo-Pascals), observed routinely in glacier and ice sheet environments, ice deforms primarily through the mechanism of dislocation creep. In dislocation creep, defects in the ice cause a discontinuity in the crystal structure (dislocations), and allow for the ice's crystal bonds to break slowly over time and form new dislocations, resulting in the slow creeping motion of ice (Duval and others, 2010). Following the discussion of Cuffey and Paterson (2010) on crystal deformation, the strain rate ϵ resulting from dislocation glide, a primary mechanism of dislocation creep, can be written as:

$$\epsilon_c = b^* \rho_d v_d, \tag{1.1}$$

where b^* is a coefficient related to the lattice offset from a single dislocation, ρ_d is the length of linear dislocation per unit volume, and v_d is the dislocation velocity. ρ_d and v_d both vary with stress according to power laws, leading to the assertion that

strain rate is linearly proportional to stress in the form of:

$$\epsilon \propto \tau^n, \tag{1.2}$$

where τ is the deviatoric stress tensor and n is the flow law exponent. The effective viscosity of ice η can be defined by writing the relationship between strain rate as stress as:

$$\tau_{jk} = 2\eta\epsilon_{jk}. \tag{1.3}$$

In this manner, ice can be modeled as a non-Newtonian fluid. Typically, this flow rheology is represented through an empirical relationship known as Glen's flow law, which defines the viscosity of ice as:

$$\eta = \frac{B}{2}\epsilon_e^{\frac{1}{n}-1}, \tag{1.4}$$

where B is a temperature dependent constant, ϵ_e is the effective strain rate, and n is the Glen's flow law exponent, typically set equal to 3 based on observations. The effective strain rate is defined as a sum over the individual components of the strain rate tensor ϵ by:

$$\epsilon_e = \sqrt{\epsilon_{ij}\epsilon_{ij}/2}. \tag{1.5}$$

This is combined with the momentum balance for fluid flow:

$$\vec{\nabla} \cdot \sigma + \rho_i \vec{g} = \rho_i \frac{D\vec{u}}{Dt}, \tag{1.6}$$

and the definition of the Cauchy stress tensor σ:

$$\sigma = 2\eta\epsilon - pI, \tag{1.7}$$

to model ice as a fluid. ρ_i denotes the density of ice, $\vec{g}$ the acceleration due to gravity, $\vec{u}$ the ice velocity, p the pressure, and I the identity tensor.

However, ice can also be thought of as a brittle solid. At sufficiently high stresses and strain rates, the material cannot sufficiently dissipate stress through slow creeping flow. In this case, brittle fracture occurs, ice separates to form gaps in the material known as crevasses, and, if crevasses fully penetrate through the ice, ice detaches from the glacier in a process known as calving. This calved glacier ice is known as an iceberg.

Glacier ice can fail under multiple modes of failure. The simplest and most commonly modeled mode is tensile failure, where extensional stress within the glacier overcomes internal cohesion and opens a crevasses. Calving also occurs due to shear failure, where shear stress overcomes the material strength and internal friction and causes a diagonal crack to open. The importance of shear failure is a hotly debated topic in the context of a process known as the marine ice cliff instability, originally proposed by Bassis and Walker (2012).

The marine ice cliff stability proposes that if glacier cliffs become too high, the cliff will fail under shear failure, exposing a higher cliff with even larger shear stresses, leading to runaway calving retreat. The unknown importance of including the marine ice cliff instability remains a large source of uncertainty in mass loss projected by climate models (Edwards and others, 2021; DeConto and others, 2021). Developing new models that include multiple modes of failure, including shear failure, is crucial to inform the importance of shear calving mechanisms to glacier mass loss.

1.3 Modeling ice at different scales

When modeling the dynamics of glaciers and ice sheets, efforts are made on a range of temporal and spatial scales to improve understanding of processes and eventually make long-term predictions that can be used when considering social and political action. In addition to glacier flow and calving, a number of additional factors operating on multiple timescales may be considered that affect overall glacier behavior. Some of these factors include atmospheric temperatures, snowfall, and ocean temperatures. Depending on the complexity of the model, weather patterns, atmospheric circulation, and ocean circulation may be considered as well. Each of these factors come with their own set of difficulties, approximations, and computational costs. In many cases it can be beneficial to forego complexity in favor of probing the effects of a few isolated processes.

1.3.1 Glacier flow

Many classes of models with varying level of approximations exist to model the flow of glaciers and ice sheets. Some examples include the shallow ice approximation, the shallow shelf approximation, and full Stokes. This list spans from extremely simplified idealistic models that neglect most components of stress to a complete balance of all stresses acting on the glacier.

The shallow ice approximation assumes that the ratio of the thickness to length of the ice mass is small, and neglects longitudinal and transverse stresses in addition to vertical stress gradients. This effectively simplifies the problem to a balance between gravitational driving stress and drag from the glacier bed. This type of approximation has extremely low computational demand and works well for the slow flowing portions of ice sheet interiors. However, it does not perform well for fast

flowing regions or in regions that transition from grounded to floating ice.

The shallow shelf approximation is well suited to model ice shelves, which are completely floating and not in contact with the bed. In this case, shear stress along the bottom of the ice shelf is zero and longitudinal stresses dominate the solution. This model is two-dimensional and does not resolve vertical gradients in velocity. Although this performs well for ice shelves, like the shallow ice approximation, it does not perform well in regions of transition from grounded to floating ice.

Higher order models exist that relax the approximations made in the shallow ice and shallow shelf approximations. However, as approximations are relaxed, computational efficiency decreases and so models must be careful to balance model resolution and accuracy with computational feasibility.

Naturally, more simplified models with many approximations are well-suited for modeling large glaciers or ice sheets or domains over a long period of time where computation time is a key concern. In contrast, full Stokes models, which retain all terms in the stress balance, are well-suited for idealized models that seek to understand the underlying fundamentals of glacier processes or for simulations of individual glaciers over a limited range of time. In the our work, a full Stokes model is used to better understanding the process of glacier calving.

1.3.2 Glacier calving

Calving happens on a time scale of seconds to minutes that is much faster than the time it takes for a glacier to flow a significant distance. Models that run on short timescales to resolve the propagation of individual crevasses within the ice are highly computationally expensive and are not feasible to run for months or years to encompass glacier flow as well (Tsai and Rice, 2010; Benn and others, 2017). In contrast, parameterizations of calving for use in lower resolution models that can

run over larger areas and longer time periods do not behave uniformly for different environments and have high uncertainties (Choi and others, 2018). Development of models at intermediate scales is helpful for bridging the gap in understanding and identifying macroscopic properties that can be used to parametrize calving in future models.

Thus, instead of relying on high resolution fracture models, it is beneficial to have a model that resolves glacier flow on longer timescales while also being able to predict calving behavior based on more macroscopic properties. The purpose of this work is to develop a model that can predict both glacier flow and fracture with low enough computational demand to run on year to decade timescales.

1.4 Existing parameterizations of calving

Although there is no agreed upon best parameterization of calving to include in ice flow and fracture models, there have nonetheless been many attempts to develop calving criteria for inclusion with flow models. For example, Choi and others (2018) compared the predictions of four existing calving laws on Greenland glaciers: height above buoyancy, eigencalving, crevasse depth, and von Mises tensile stress. The implementations of these calving laws by Choi and others (2018) provide two different types of predictions depending on the law being tested. Height above buoyancy and crevasse depth determine the location of the calving front, while eigencalving and von Mises tensile stress predict a calving rate that factors into calculation of the ice terminus. These laws predict calving behavior through varied criteria on the ice geometry, internal strain rate, and internal stress. However, predictions are not necessarily consistent with one another and often need to be calibrated for particular glaciers to match observations.

Other studies have approached simulating calving through damage mechanics, which allows for the advection of damaged ice through the domain as ice flows (Pralong and Funk, 2005; Borstad and others, 2012; Duddu and others, 2013; Krug and others, 2014; Jiménez and others, 2017). This is of great benefit because observations show that advection is crucial in predicting the state of crevasses within a glacier (Mottram and Benn, 2009; Enderlin and Bartholomaus, 2020). However, these implementations are also empirical, depend on parameterizations that are difficult to constrain, and can be computationally demanding to implement for long times scales spanning years to decades.

An existing simple, stress-based criterion to predict calving is known as the Nye zero stress criterion. This criterion assumes that tensile crevasses extend to the depth in the glacier where the extensional internal stress vanishes and becomes compressive. This effectively assumes a zero yield strength of ice - it has no internal cohesion. While real glacier ice certainly has a nonzero yield strength, laboratory experiments on ice give values that are difficult to reconcile with observations and possible values for yield strength are also difficult to constrain. Therefore, while simplistic, the Nye zero stress criterion can provide a useful upper bound on calving rates. Furthermore, studies that use the Nye zero stress criterion have been able to reproduce behavior consistent with observations (Nick and others, 2010; Todd and Christoffersen, 2014), demonstrating its usefulness as a calving criterion. Due to the simplicity of the Nye zero stress criterion, we use this criterion as the starting point for model development and seek to improve on it by adding advection of tensile crevasses and mixed mode failure.

1.5 Our mixed mode full Stokes calving model

Initially, full Stokes flow, the Nye's zero stress criterion, and crevasse advection are combined to leverage the simplicity of the Nye's zero stress criterion and the insight into ice history given by advection. Developing this model also provides valuable and novel insight into careful numerical and computational considerations for modeling calving. Our model is tested on a variety of ice temperatures, frictional properties of the bed, and bed shapes.

Subsequently, we improve our model by adding shear failure and basal melt. By adding shear failure, we allow for another mode of rapid brittle failure in the ice that is caused by excessive compressive stress rather than extensional stress. This is particularly important as it is the driving mechanism behind the controversial marine ice cliff instability (Bassis and Walker, 2012). Basal melt, the melting of ice at the bottom of the glacier through contact with warmer ocean water, is another crucial mass loss mechanism for glaciers, which can also influence calving behavior (Ma and Bassis, 2019). By adding these additional and interacting mechanisms for further mass loss, our model captures a wider range of possible glacier behaviors.

1.6 Numerical implementation

Our glacier model is written in Python using the open-source finite element library FEniCS (Alnæs and others, 2015) and leveraging the LEoPart library (Maljaars and others, 2020) for advection of crevasse data. Developing the model using FEniCS provides a high level of customization and control over development when compared to existing full Stokes glacier models such as Elmer-Ice (Gagliardini and others, 2013).

1.6.1 The finite element method

The finite element method is a numerical approach used to solve a range of scientific problems, including those in glacier flow. In our model, we apply the standard procedure for incompressible full Stokes flow with the re-addition of the acceleration term of the momentum balance for numerical stability as will be discussed further in Chapter II.

We start with the momentum balance given in Equation 1.6 along with the condition for incompressibility written as:

$$\vec{\nabla} \cdot \vec{u} = 0. \tag{1.8}$$

The set of differential equations written in their standard form in Equation 1.8 and Equation 1.6 are referred to as the strong form of the equations.

To transform the strong form of the differential equations into their corresponding weak form, which can be solved using the finite element method, we first write Equation 1.6 as a function of the two unknown variables, the vector velocity $\vec{u}$ and the scalar pressure p. Using Equation 1.7, Equation 1.6 can be rewritten as:

$$\vec{\nabla} \cdot (2\eta(\vec{u})\epsilon(\vec{u})) - \vec{\nabla} p + \rho_i \vec{g} = \rho_i \frac{D\vec{u}}{Dt}, \tag{1.9}$$

where $\eta(\vec{u})$ is the viscosity defined in Equation 1.4 and $\epsilon(\vec{u})$ is the strain rate tensor defined via:

$$\epsilon(\vec{u}) = \frac{1}{2}\left(\left(\vec{\nabla}\vec{u}\right) + \left(\vec{\nabla}\vec{u}\right)^{\mathrm{T}}\right). \tag{1.10}$$

To transform the strong form of Equation 1.9 into its corresponding weak form, we multiply Equation 1.9 by a velocity test function $\vec{v}$. We then perform a volume integral (dV) over the entire domain of interest Ω to find:

$$\int_\Omega \vec{\nabla} \cdot (2\eta(\vec{u})\epsilon(\vec{u})) \cdot \vec{v}\, dV - \int_\Omega \vec{\nabla} p \cdot \vec{v}\, dV + \int_\Omega \rho_i \vec{g} \cdot \vec{v}\, dV = \int_\Omega \rho_i \frac{D\vec{u}}{Dt} \cdot \vec{v}\, dV. \tag{1.11}$$

Next, we rewrite the first two terms in Equation 1.11 using the product rule of differentiation to:

$$\int_\Omega \vec{\nabla} \cdot (2\eta(\vec{u})\epsilon(\vec{u})) \cdot \vec{v}\, dV = -\int_\Omega (2\eta(\vec{u})\epsilon(\vec{u})) \cdot \vec{\nabla} v\, dV + \int_\Omega \vec{\nabla} \cdot (2\eta(\vec{u})\epsilon(\vec{u}) \cdot \vec{v})\,, \tag{1.12}$$

and:

$$-\int_\Omega \vec{\nabla} p \cdot \vec{v}\, dV = \int_\Omega p\vec{\nabla} \cdot \vec{v}\, dV - \int_\Omega \left(\vec{\nabla} \cdot (p\vec{v})\right) dV. \tag{1.13}$$

The divergence theorem can be used to rewrite the final terms in Equation 1.12 and Equation 1.13 as surface integrals (dS) on the domain boundary $\partial\Omega$:

$$\int_\Omega \vec{\nabla} \cdot (2\eta(\vec{u})\epsilon(\vec{u})) \cdot \vec{v}\, dV = -\int_\Omega (2\eta(\vec{u})\epsilon(\vec{u})) \cdot \vec{\nabla} v\, dV + \int_{\partial\Omega} (2\eta(\vec{u})\epsilon(\vec{u})) \cdot \hat{n} \cdot \vec{v}\, dS \tag{1.14}$$

and:

$$-\int_\Omega \vec{\nabla} p \cdot \vec{v}\, dV = \int_\Omega p\vec{\nabla} \cdot \vec{v}\, dV - \int_{\partial\Omega} p\vec{v} \cdot \hat{n}\, dS, \tag{1.15}$$

where $\hat{n}$ is the unit normal vector.

Plugging in Equation 1.14 and Equation 1.15 into Equation 1.11 leads to the weak form of the partial differential equation:

$$\begin{aligned} -\int_\Omega (2\eta(\vec{u})\epsilon(\vec{u})) \cdot \vec{\nabla} v\, dV + \int_{\partial\Omega} (2\eta(\vec{u})\epsilon(\vec{u})) \cdot \hat{n} \cdot \vec{v}\, dS + \int_\Omega p\vec{\nabla} \cdot \vec{v}\, dV - \int_{\partial\Omega} p\vec{v} \cdot \hat{n}\, dS \\ + \int_\Omega \rho_i \vec{g} \cdot \vec{v}\, dV = \int_\Omega \rho_i \frac{D\vec{u}}{Dt} \cdot \vec{v}\, dV. \end{aligned} \tag{1.16}$$

Similarly, the incompressibility condition expressed in Equation 1.8 is multiplied by a pressure test function q and integrated over the entire domain to obtain:

$$\int_\Omega q\vec{\nabla} \cdot \vec{u}\, dV = 0. \tag{1.17}$$

Equation 1.17 is added to equation 1.16 to complete the variational form. This equation holds for any set of test functions $\vec{v}$ and q as long as the original functions

$\vec{u}$ and p satisfy the differential equation. While the original strong form of the differential equation must be true at every point in the domain, the weak form only holds in an integrated, averaged sense.

1.6.2 FEniCS implementation

The weak form of the problem expressed in Equation 1.16 and Equation 1.17 is implemented and solved in the open-source finite element library FEniCS (Alnæs and others, 2015). The user-friendly Python interface of FEniCS allows for specification of the variational form for the differential equation to be solved, boundary conditions, mesh, and function spaces. Once the problem is specified, DOLFIN, the C++ and Python problem solving environment for differential equations in FEniCS, handles the numerical solution.

The solution to Equation 1.16 can be approximated by a discrete solution using the finite element method. First, the full domain Ω is divided into a number of N sub-domains Ω_i with M nodes each. Thus, an integral of any function $g(\vec{u}, p)$ over the entire domain Ω can be represented by a sum of integrals over each sub-domain as:

$$\int_{\Omega} g(\vec{u}, p)\, dV \approx \sum_{i=1}^{N} \left(\int_{\Omega_i} g(\vec{u}, p)\, dV \right). \tag{1.18}$$

The solutions for velocity and pressure are also discretized over a sum of basis functions. For example, the solution for pressure can be written as:

$$p \approx \sum_{j=1}^{M} U_j \phi_j, \tag{1.19}$$

where U_j are shape functions and ϕ_j are basis functions summed over the nodes in each sub-domain Ω_i. Basis functions must be carefully chosen to achieve stability when solving a particular problem, and there are a variety of choices for basis functions available and supported by FEniCS. In this work, we use either Continuous

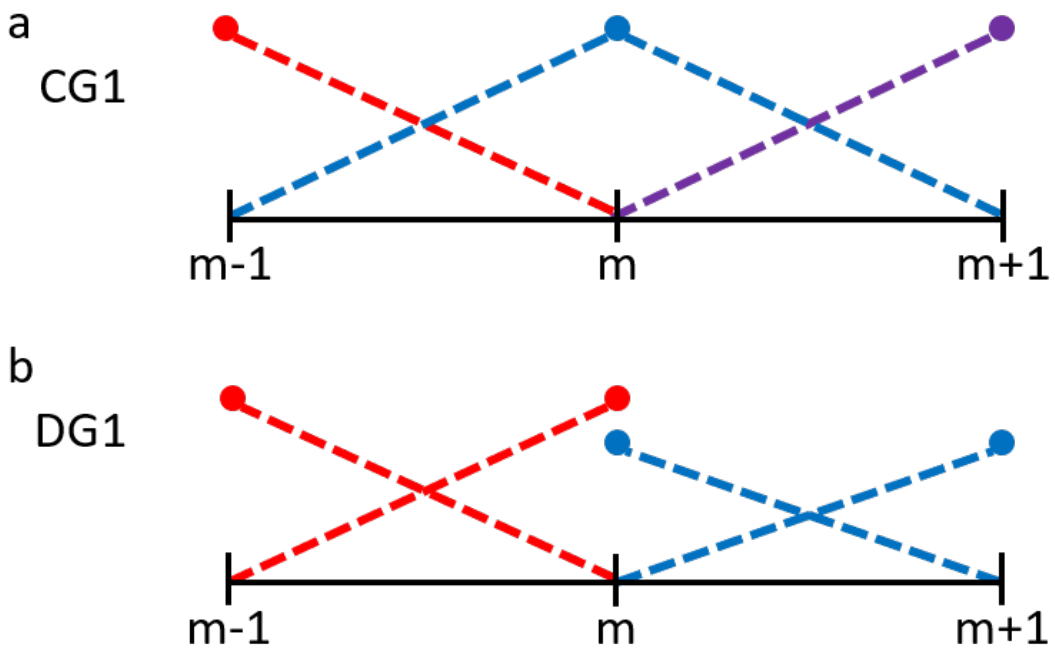

Figure 1.1: Illustration of basis functions near the m-th node in one dimension for first order Continuous Galerkin (a) and first order Discontinuous Galerkin (b) finite element spaces. Dashed colored lines indicate different first order polynomial basis functions and colored dots indicate nodal values of polynomials. The CG space has continuous values across nodes while the DG space is discontinuous.

Galerkin or Discontinuous Galerkin finite elements, which correspond to continuous or discontinuous piecewise polynomial basis functions, respectively.

Figure 1.1 shows the differences between a first order Continuous Galerkin (CG1) and a first order Discontinuous Galerkin (DG1) finite element space. In a CG1 space, values are continuous across nodes, with linear basis functions contributing to two neighboring cells. In contrast, for a DG1 space, values are discontinuous across nodes, with different functions approximating each cell.

To ensure a stable discretization of the problem, Taylor-Hood elements are chosen as the basis for the velocity and pressure solutions (Helanow and Ahlkrona, 2018). Taylor-Hood elements consist of a second order Continuous Galerkin (CG2) space for velocity and a CG1 space for pressure. Diagnostic stresses and strains are calculated

from velocity and pressure solutions and projected to a DG1 space when necessary.

1.6.3 Meshing

An unstructured triangular mesh is generated using the open-source meshing software Gmsh (Geuzaine and Remacle, 2009) and imported into FEniCS after being saved as an .xml file. Using Gmsh allows for finer control over mesh resolution and structure than the meshing tools available in FEniCS. For example, areas of different mesh resolutions can be specified, increasing mesh resolution near regions of interest to improve numerical accuracy and decreasing mesh resolution elsewhere to maintain computational efficiency. Our mesh is Langrangian and corresponds to the domain of the glacier. At each time step, the existing mesh is moved based on the velocity solution to reflect the new glacier location. However, a new mesh is generated if the model predicts a calving event, drastically changing the glacier (and mesh) domain, or if the ratio of minimum to maximum finite element radii drops below 0.1 according to the FEniCS MeshQuality class. The latter prevents numerical issues due to highly distorted finite elements.

1.6.4 Advection

So that information on ice history can be retained after remeshing, ice properties are advected using LEoPart (Maljaars and others, 2020), a particle tracking library developed for integration with FEniCS. Using LeoPart, a set of particles is generated and distributed randomly throughout the finite element mesh with a set number of particles per element. Using LEoPart, data on velocity and stress can be interpolated between the particles and the mesh while limiting numerical diffusion.

CHAPTER II

Time Step Dependence (and Fixes) in Stokes Simulations of Calving Ice Shelves

This chapter appears in its entirety in the following:

Berg B and Bassis J (2020) Brief communication: Time step dependence (and fixes) in stokes simulations of calving ice shelves. *The Cryosphere*, **14**, 3209–3213 (doi: 10.5194/tc-14-3209-2020)

2.1 Introduction

Stokes simulations are used in glaciology as a tool to determine the time evolution of glaciers (e.g., Gagliardini and others, 2013). Increasingly, these models are also used to examine the stress field within glaciers to better understand factors that control crevasse formation and the onset of calving events (Ma and others, 2017; Benn and others, 2017; Nick and others, 2010; Todd and Christoffersen, 2014; Ma and Bassis, 2019). This type of model can provide insight into the relationship between calving, climate forcing, and boundary conditions (e.g., Todd and Christoffersen, 2014; Ma and others, 2017; Ma and Bassis, 2019).

Here we show that a common method used to implement the ice-ocean boundary condition in Stokes models can result in solutions that are unphysically sensitive to

the choice of simulation time step size. This behavior manifests in applications that allow for rapid changes in the model domain — a type of change associated with models that allow for instantaneous calving events or crevasses (Todd and Christoffersen, 2014; Todd and others, 2018; Yu and others, 2017). The time step dependence arises because for glaciers outside of hydrostatic equilibrium, the acceleration is not small as assumed in Stokes flow. We illustrate both the issue and the solution using an idealized ice shelf geometry (Fig. 2.1) where the upper portion has calved away, emulating the "footloose" mechanism proposed by Wagner and others (2014) where an aerial portion of the calving front first detaches.

2.2 Problem Description

2.2.1 Glacier Stress Balance

Denoting the velocity field in two dimensions by $\vec{u}(x,z,t) = (u_x(x,z,t), u_z(x,z,t))$ and pressure by $P(x,z,t)$, conservation of linear-momentum can be written in the form:

$$\vec{\nabla} \cdot \vec{\sigma} + \rho_i \vec{g} = \rho_i \frac{D\vec{u}}{Dt}, \tag{2.1}$$

where D/Dt denotes the material derivative. The Cauchy stress is defined in terms of strain rate, effective viscosity, pressure, and the identity matrix $\vec{I}$:

$$\vec{\sigma} = 2\eta\vec{\epsilon} - P\vec{I}, \tag{2.2}$$

with strain rate tensor $\vec{\epsilon}$ given by:

$$\vec{\epsilon}_{ij} = \frac{1}{2}\left(\frac{\partial u_i}{\partial r_j} + \frac{\partial u_j}{\partial r_i}\right). \tag{2.3}$$

Here ρ_i is the density of ice, $\vec{g}$ is the acceleration due to gravity, and η is the effective viscosity of ice:

$$\eta = \frac{B}{2}\epsilon_e^{\frac{1}{n}-1}. \tag{2.4}$$

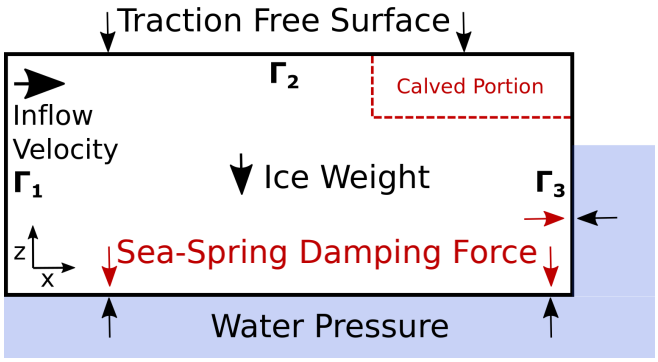

Figure 2.1: A diagram showing the boundary conditions of an idealized floating ice shelf. The ice-ocean interface is subject to two normal stresses - the depth dependent water pressure and the numerical damping force for stabilization to hydrostatic equilibrium. The dashed red line illustrates an iceberg that breaks off from the top of the calving front (exaggerated), reducing the freeboard and instantaneously perturbing the ice shelf from hydrostatic equilibrium.

The effective viscosity is a function of the effective strain rate $\epsilon_e = \sqrt{\vec{\epsilon}_{ij}\vec{\epsilon}_{ij}/2}$, a temperature dependent constant B, and the flow-law exponent $n = 3$.

In the Stokes approximation, we drop the acceleration term on the right hand side of Eq. (2.1), which is justified for most glaciological applications (e.g., Greve and Blatter, 2009). However, as we shall show, this assumption is problematic for applications where the ice rapidly departs from hydrostatic equilibrium.

2.2.2 Boundary Conditions

To illustrate an example where the Stokes flow problem rapidly departs from hydrostatic equilibrium, we consider a two-dimensional floating ice shelf (Fig. 2.1). Along the inflow portion of the domain (Γ_1), shear traction vanishes and we specify the normal component of the velocity $\vec{u} \cdot \hat{n} = u_1$, where u_1 is a constant and $\hat{n}$ is the normal vector along Γ_1. At the ice-atmosphere boundary (Γ_2) we assume the surface is traction free. At the boundary between ice and ocean (Γ_3) the shear traction along the ice-interface vanishes and continuity of normal traction along the ice-ocean interface can be written as $\sigma_{nn}(x,t) = -\rho_w g b(x,t)$ where $b(x,t)$ is the position of the

ice-ocean interface.

Problems arise with this form if the glacier is not *exactly* in hydrostatic equilibrium because buoyancy forces along the ice-ocean interface cannot be balanced by internal stresses. In this case, there is no unique solution. In reality, of course, inertial effects are not negligible and the ice will quickly re-adjust to hydrostatic equilibrium as a consequence of buoyant uplift through the (nearly) inviscid ocean.

We can more appropriately specify the boundary condition for Stokes flow at the ice-ocean interface by writing it in the form:

$$\sigma_{nn}(x,t) = -\rho_w g\,[b(x,t) + \Delta z(x,t)] \quad \text{on} \quad \Gamma_3 \tag{2.5}$$

where $\Delta z(x,t)$ is an *a priori* unknown isostatic adjustment that could potentially include a rigid body translation and, for a freely floating iceberg, rigid body rotation. Crucially, the rigid body motion must be determined as part of the solution to enable the local and global force balance to close.

The additional isostatic adjustment term Δz has a simple physical explanation: if normal stress was exactly hydrostatic, $\sigma_{nn} = \rho_i g H$ where H is the ice shelf thickness. Equation (2.5) can then be solved for Δz to determine the position of the bottom interface needed for the forces to balance, which is exactly what is done in the shallow shelf approximation. The full Stokes approximation is more complex as internal stresses also contribute to the normal stress at the ice-ocean interface, but the location of the ice-ocean interface needs to be solved for as part of the solution to the problem, which we examine next.

2.2.3 Numerical Stabilization of Buoyant Uplift

Different numerical methods use different techniques to estimate Δz in Eq. (2.5). For example, in Elmer/Ice, a popular package for modeling Stokes glacier flow, Du-

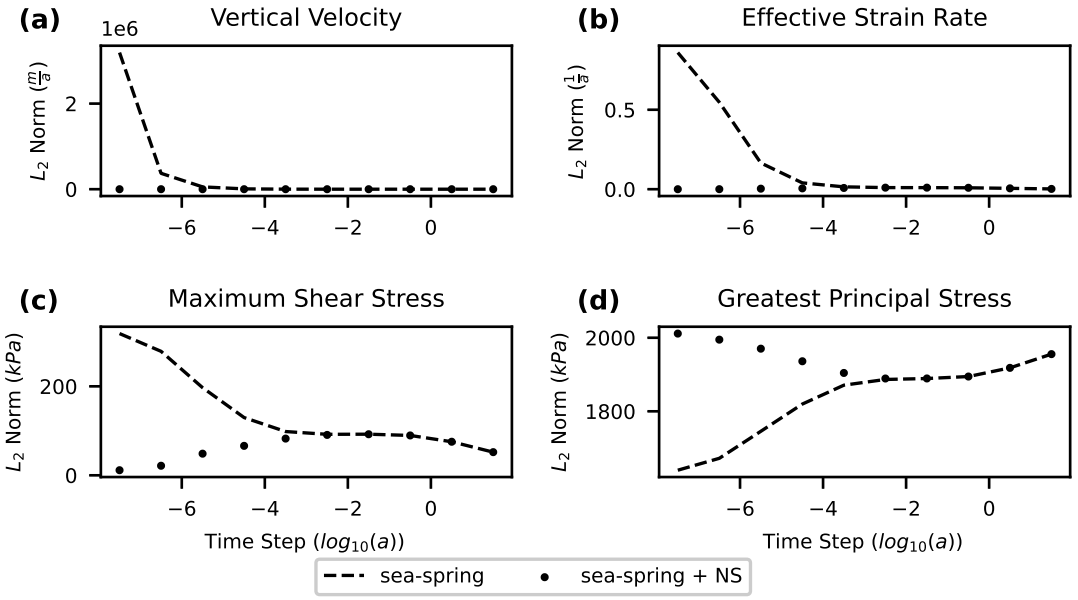

Figure 2.2: L_2 norm of **(a)** vertical velocity, **(b)** effective strain rate, **(c)** maximum shear stress, and **(d)** greatest principal stress immediately after the emulated calving event. The norm is calculated based on cell-averaged values. Solutions after a single time step are shown for sea-spring damping and sea-spring with Navier Stokes (NS) for time step size ranging from 1 second to 30 years. The sea-spring with Navier Stokes term gives physical solutions for all time steps but still shows variability with time step consistent with the evolution of the system.

rand and others (2009) proposed an ingenious solution in which Δz is estimated based on a Taylor series of vertical position of the ice-ocean interface:

$$\Delta z = u_z(x,t)\Delta t + O(\Delta t^2). \tag{2.6}$$

This Taylor series transforms the isostatic adjustment into a time step-dependent Newtonian velocity damping:

$$\sigma_{nn}(x,t) = -\rho_w g \left[b(x,t) + u_z(x,t)\Delta t \right]. \tag{2.7}$$

Here, the velocity u_z can include rigid body translation. The coefficient of the damping force in this approximation is proportional to the time step size Δt and vanishes in the limit of small Δt. We refer to the damping method given in Eq. (2.7) as the "sea-spring" method based on the nomenclature used in Elmer/Ice documentation.

We illustrate the time step dependence using a floating ice shelf as an example. In this case, global force balance is not guaranteed, leading to a formally ill-posed problem. However, the lack of a solution (which results in an exceptionally large velocity using the sea-spring stabilization) persists even when grounded ice is included in the domain because the velocity (and strain rate) solution can become unphysically sensitive to the position of the ice-ocean interface.

2.3 Calving-Based Convergence Test

For our test, we implement an idealized rectangular ice shelf of thickness 400 m and length 10 km. This ice shelf is initialized to be in exact hydrostatic equilibrium. We set the inflow velocity for the upstream boundary condition to 4 km a^{-1}. These thickness and velocity parameters are broadly consistent with observations for the last 10 km of Pine Island ice shelf (Rignot and others, 2017, 2011; Mouginot and others, 2012; Paden and others, 2010). The temperature dependent constant in Glen's flow law is chosen to be 1.4×10^8 Pa $s^{\frac{1}{3}}$, the value given by Cuffey and Paterson (2010) for $-10°C$.

To emulate the occurrence of a calving event that would perturb the ice shelf from hydrostatic equilibrium, a rectangular section of length 50 m and thickness 20 m is removed from the upper calving front of the glacier (Fig. 2.1). This type of calving behavior has been proposed as the trigger of a larger calving mechanism related to buoyant stresses on the ice shelf (Wagner and others, 2014). The numerical effects we document are not unique to this style of calving and this mechanism is only meant to illustrate the numerical issues.

The problem is implemented in FEniCS (Alnæs and others, 2015), an open source finite element solver with a Python interface that has been previously used for Stokes

glacier modeling (Ma and others, 2017; Ma and Bassis, 2019). The problem is solved using an Arbitrary Lagrangian-Eulerian formulation using mixed Taylor-Hood elements with quadratic elements for velocity and linear elements for pressure. The open source finite element mesh generator Gmsh is used to generate a unstructured mesh with uniform grid spacing of 10 m near the calved portion of the domain and grid spacing of 40 m elsewhere.

In Fig. 2.2, we show the L_2 norm of vertical velocity, effective strain rate, maximum shear stress, and greatest principle stress immediately after the calving event, but computed using different values for Δt in Eq. (2.7). This shows the sensitivity of the vertical velocity, effective strain rate, maximum shear stress, and greatest principal stress to time step size when using the sea-spring boundary condition. In addition to the behavior of the L_2 norm, we also examine the maximum value of the maximum shear stress and greatest principal stress (Fig. 2.3). Maximum values may be a better predictor of the effect of time step dependence on the results of Stokes calving models. Because calving models often assume that calving is likely if a stress threshold is exceeded (Ma and others, 2017), outliers in stress are more important than a stress averaged over the entire domain.

2.4 Proposed Solution - Reintroduce Acceleration Term into Stress Balance

The velocity solution is unphysical because the neglected acceleration term is not actually small relative to the other terms in Eq. (2.1). This is because large velocities associated with hydrostatic adjustment rapidly change on time scales that are short compared to the internal deformation of the ice. It may be possible to separate a rigid body translation and rotation that satisfies global force and torque balance from the

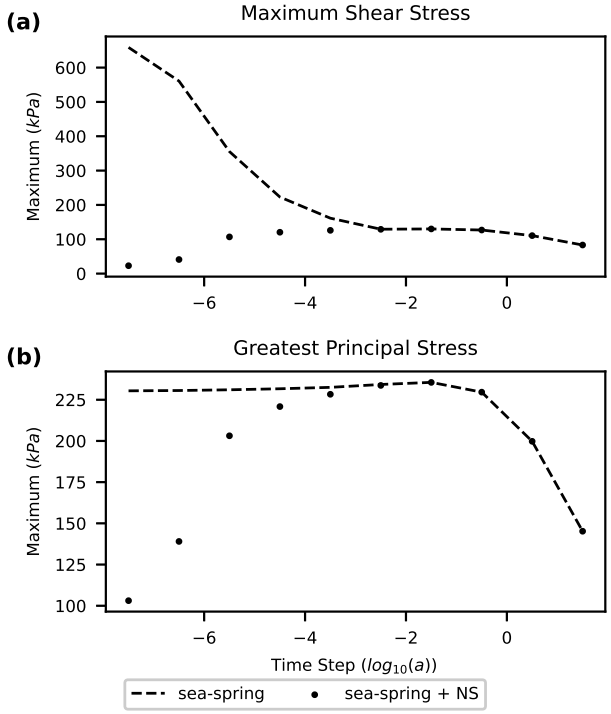

Figure 2.3: Maximum **(a)** maximum shear stress and **(b)** greatest principal stress immediately after the emulated calving event. The maximum is calculated based on cell-averaged values. Solutions after a single time step are shown for sea-spring damping and sea-spring with Navier Stokes (NS) for time step size ranging from 1 second to 30 years. Without corrections, maximum stress is overestimated in the Stokes model, which could lead to overestimation of glacier retreat due to calving.

internal deformation, but this quickly becomes cumbersome and impractical when we include the potential for ice to break: global force and torque balance would have to be maintained on each intact portion of ice. Instead, we reintroduce the acceleration term directly to the Stokes equation and show that this regularizes the solution for small time steps. We use a simple first order backwards differentiation scheme in a Lagrangian reference frame:

$$\frac{D\vec{u}_i}{Dt} = \frac{\vec{u}_i - \vec{u}_{i-1}}{\Delta t}, \tag{2.8}$$

where $\vec{u}_i$ and $\vec{u}_{i-1}$ denote the velocity of Lagrangian fluid parcels at the current time step and the velocity at the previous time step, respectively. In the example

considered here, the fixed horizontal velocity at the upstream boundary does not permit rigid body rotation and Eq. (2.8) remains a valid approximation even in a Eulerian coordinate system. As an initial condition on velocity, we assume a uniform velocity field of 4 km a^{-1} (equal to the inflow velocity) in the horizontal direction and zero in the vertical direction. The choice of zero initial velocity in the vertical direction is consistent with the idea that the ice shelf has instantaneously been perturbed from hydrostatic equilibrium.

Restoring the inertial term effectively introduces a Newtonian damping term on the entire body of the glacier where the damping coefficient is $C = 1/\Delta t$. Computational difficulty is not impacted by reintroducing the acceleration term in this way because the term is linear with respect to velocity. However, unless a fully implicit scheme was implemented, the solution becomes inaccurate (and unstable) for long time steps. Therefore, we propose to use both damping terms so that the system of equations is numerically accurate for all time step sizes.

When we include both damping terms, vertical velocity, effective strain rate, maximum shear stress, and greatest principal stress maintain physical values for both small and large time steps (Fig. 2.2). At small time steps the acceleration term dominates and the sea-spring with Navier Stokes solution departs from the sea-spring solution. In this limit, the (nearly) rigid body isostatic adjustment of the ice shelf dominates the solution. By contrast, for large time steps, the sea-spring damping dominates and the two methods overlap. At intermediate time steps, both damping terms contribute as the solution transitions from the regime dominated by inertial effects to one where inertial effects are small. It is crucial to note that although the sea-spring with Navier Stokes solution retains time step dependence for small time steps, the time step dependence now results from the physical evolution of the

system: the solution resolves the acceleration and deceleration of the glacier as it bobs up-and-down in the ocean and approaches a steady-state.

Although the sea-spring solution shows a smaller L_2 norm of greatest principal stress than the sea-spring with Navier Stokes solution, this is due to large *negative* compressive stresses associated with being outside of hydrostatic equilibrium. If we instead examine the maximum of the stress fields, the sea-spring solution shows larger values for both maximum shear stress and greatest principal stress (Fig. 2.3). This is particularly evident for the maximum shear stress, which is overestimated by an order of magnitude at the shortest time step tested. In the footloose calving mechanism, when a portion of the upper calving front is removed, the front of the ice shelf becomes buoyant and produces increased shear stress upstream on the ice shelf (Wagner and others, 2014). This over prediction of stresses could cause a calving model to predict unphysical calving events due to numerical inaccuracies.

2.5 Conclusions

Our study shows that using a common numerical stabilization method of the ice-ocean boundary in Stokes glacier modeling there is an explicit time step dependence of the solution that is unphysical for small time steps when the domain rapidly departs from hydrostatic equilibrium. For model applications where changes in the domain are only due to viscous flow, the time step dependence is not problematic as long as domains are (nearly) in hydrostatic equilibrium at the start of simulation. However, for applications where rapid changes to the model domain occur, such as when calving rules are implemented, sudden departure from hydrostatic equilibrium is not only possible, but expected. In these cases, time step dependence of the solution will appear. This can contaminate solutions of the stress after calving,

potentially leading to a cascade of calving events and an overestimate of calving flux if numerical artifacts are not addressed. However, the time step dependence can be easily cured with little computational cost by reintroducing the acceleration term to the Stokes flow approximation. The acceleration term regularizes the solution for small time step sizes and provides consistent solutions for all time steps.

CHAPTER III

Impact of Tensile Crevasse Advection and Shear Localization on Glacier Calving Behavior

This chapter is a manuscript currently under review for publication in the *Journal of Glaciology*.

3.1 Introduction

Calving is one of the largest sources of uncertainty in projected mass loss from ice sheets and glaciers (Stocker and others, 2013; Pörtner and others, 2019; Pattyn and Morlighem, 2020) and developing better models of the calving process is essential for accurate sea level projections. Current parameterizations of calving, such as height above buoyancy (Vieli and others, 2001), eigencalving (Levermann and others, 2012), or von Mises stress (Morlighem and others, 2016) can replicate behavior of glacier advance and retreat in some cases, but the predictions made by these parameterizations often need to be tuned to match glacier behavior and result in projections of rates of mass loss that diverge over time (Choi and others, 2018).

The Nye zero stress criterion provides a simple method to introduce a physically motivated parameterization of calving into glacier models (Nye, 1957; Nick and others, 2010; Todd and Christoffersen, 2014; Ma and others, 2017; Ma and Bassis,

2019). This criterion assumes crevasses penetrate to the depth in the glacier where the largest effective principle stress vanishes. This method is computationally cheap to incorporate into models and straightforward to implement compared to other theories that can be cumbersome to include in ice sheet models, such as linear elastic fracture mechanics (Krug and others, 2014; Yu and others, 2017; Jiménez and Duddu, 2018).

Previous crevasse depth studies, however, omit the effect of crevasse advection despite the fact that observations show advection is important in predicting the location and depth of crevasses (e.g., Mottram and Benn, 2009; Enderlin and Bartholomaus, 2020). The omission of advection and the assumption that crevasses immediately "heal" makes modeled calving solely dependent on the instantaneous stress within the glacier. Although instantaneous stress near the terminus may be diagnostic of criteria for calving in some cases, it may not adequately predict calving events where ice near the terminus is highly crevassed due to upstream crevasse formation and advection.

An alternative approach to simulating fractures in ice uses damage mechanics, which can easily incorporate advection of a scalar (or tensor) damage variable (Pralong and Funk, 2005; Borstad and others, 2012; Duddu and others, 2013; Krug and others, 2014; Jiménez and others, 2017). Damage mechanics has the advantage that it is well suited to simulate the propagation of crevasses within numerical models. However, damage mechanics relies on poorly constrained empirical damage production criteria that are difficult to constrain with field or laboratory data and can be computationally expensive to implement for long time scale simulations.

Here, we formulate a calving model that combines elements of the Nye zero stress model with damage mechanics. The basis of our model is the Nye zero stress crevasse

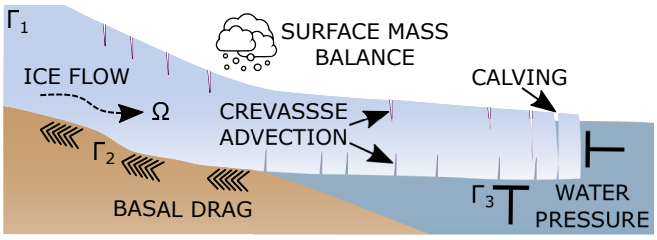

Figure 3.1: An illustration of the different processes in the calving model. Incompressible flow with indicated boundary conditions determines the viscous time evolution of the glacier. Based on the Nye zero stress criterion, tensile crevasses form and advect with the ice. A calving event occurs when surface and basal crevasses meet.

criterion. However, we generalize the Nye zero stress model to include advection of "damaged" or crevassed regions of ice along with adding the potential for shear localization. Although similar to damage based models, our model assumes that brittle failure occurs rapidly compared to the time scale of ice flow and thus portions of the ice transition immediately from "intact" to "fractured".

3.2 Model Description

We include crevasse formation and advection in a two dimensional flowline glacier model. Choosing a two dimensional representation reduces computational cost and simplifies the implementation of the calving criteria. A schematic illustration of the model is shown in Figure 3.1. The different elements are described in detail below.

3.2.1 Incompressible viscous flow

We use a modified version of the incompressible equations describing slow, viscous flow, which can be written as:

$$\begin{aligned} \nabla \cdot \left(\eta \left(\nabla \mathbf{u} + (\nabla \mathbf{u})^T \right) \right) - \nabla p + \rho \mathbf{g} &= \rho \frac{D\mathbf{u}}{Dt} \quad \text{in} \quad \Omega \\ \nabla \cdot \mathbf{u} &= 0 \quad \text{in} \quad \Omega, \end{aligned} \tag{3.1}$$

where Ω indicates the entire glacier domain. The effective viscosity is denoted by η,

the velocity vector by $\mathbf{u}(x, z, t)$, and the pressure by $p(x, z, t)$. We retain the acceleration term following Berg and Bassis (2020) as a physically based regularization that avoids unphysical time step dependence of the velocity and stress fields.

The effective viscosity of ice is calculated using Glen's flow law using a temperature dependent constant B and a flow law exponent $n = 3$:

$$\eta = \frac{B}{2}\epsilon_e^{\frac{1}{n}-1}, \tag{3.2}$$

where the effective strain rate is related to the strain rate tensor by:

$$\epsilon_e = \sqrt{\epsilon_{ij}\epsilon_{ij}/2}, \tag{3.3}$$

and we have used summation notation.

3.2.2 Boundary conditions

Denoting the upstream boundary as Γ_1 and the ice-bed interface as Γ_2, the boundary conditions on velocity are given by:

$$\begin{aligned} \mathbf{u} \cdot \hat{n} &= 0 \ \text{ on } \ \Gamma_1 \\ \mathbf{u} \cdot \hat{n} &\leq 0 \ \text{ on } \ \Gamma_2, \end{aligned} \tag{3.4}$$

where $\hat{n}$ is defined as the outward facing unit normal vector. The velocity boundary condition on Γ_1 represents a free slip boundary condition at the ice divide with zero inflow. The inequality condition on Γ_2 is a no-penetration boundary condition for grounded ice.

For simplicity, we use a modified Weertman sliding law with the drag force along the bed proportional to the cubed root of the sliding velocity. Defining Γ_3 as the

portion of the ice boundary beneath sea level, the applied stresses for basal drag and water pressure are thus given by:

$$\begin{aligned} \hat{\tau} \cdot \sigma \cdot \hat{\tau} &= -\beta |u|^{-\frac{2}{3}} (\mathbf{u} \cdot \hat{\tau}) \quad \text{on} \quad \Gamma_2 \\ \hat{n} \cdot \sigma \cdot \hat{n} &= -\rho_w g z_w \quad \text{on} \quad \Gamma_3. \end{aligned} \tag{3.5}$$

Here $\hat{\tau}$ denotes the unit vector tangential to the surface, β is the sliding coefficient, ρ_w is the density of water, and z_w is the ice depth relative to sea level.

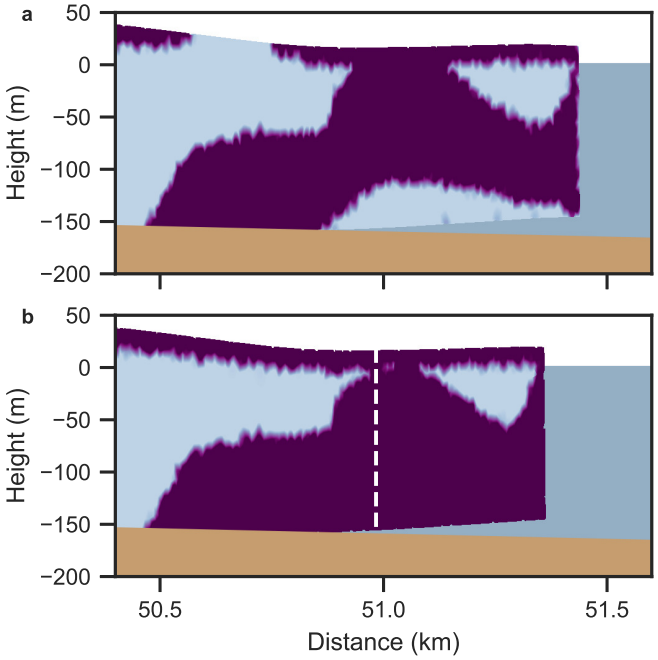

Figure 3.2: Snapshot of floating ice tongue with with purple showing crevassed ice and vertical calving indicated by a dashed white line. Model results shown without tensile crevasse advection (a) and with tensile crevasse advection (b). Slippery bed parameters as given in Table 3.1. Crevasses moving downstream from the grounding line lead to a calving event if advection is included. After a calving event occurs, all downstream ice from the calving location is removed and is no longer present in the model.

3.2.3 Crevasse penetration and calving model

We consider both purely tensile failure and shear localization. Shear localization is considered to occur on pre-existing faults and is a consequence of the instantaneous

stress within the glacier; advection of crevasses in our model is thus limited to tensile failure.

Tensile crevasse formation and advection

For tensile crevasses to form, we assume that the local stress field must satisfy the Nye's zero stress criterion (Nye, 1957). The largest effective principle stress σ_{Nye} is defined using the greatest principle stress σ_1 as:

$$\sigma_{\text{Nye}} = \sigma_1 + \rho_w g z_w. \tag{3.6}$$

We model crevasse formation and advection as a binary scalar field of "crevasses" in the ice. The crevasse field c_n at time step t_n, given by:

$$c_n = \begin{cases} 1 & \text{if } \sigma_{\text{Nye}} > 0 \text{ or } c_{n-1} = 1 \\ 0 & \text{otherwise,} \end{cases} \tag{3.7}$$

is dependent on the Nye stress exceeding zero and the crevasse field at the previous iteration. This implementation of the Nye's zero stress criterion is equivalent to the choice of a zero tensile yield strength for ice. One limitation of our approach is that we do not resolve individual crevasses, but instead consider a macroscopic "field" where regions are either fractured or intact. Moreover, our crevasse criterion effectively introduces a binary damage parameter that is zero or unity. This implies that the time scale of damage growth is fast compared to the viscous time scale. For this study, we assume crevasses are narrow brittle features that do not affect the larger scale rheology.

Once formed, crevasses persist indefinitely and, in our model, are not allowed to heal. Extended time under compressive stress may allow crevasses to close and

Table 3.1: Set of parameters used for model tests.

Parameter Set	T (°C)	β ($\mathrm{Pa\,m^{-\frac{1}{3}}\,s^{\frac{1}{3}}}$)
Baseline	-10	7.6 E6
Warm Ice	-2	7.6 E6
Slippery Bed	-10	3.8 E6
Warm Ice and Slippery Bed	-2	3.8 E6

refreeze. However, we assume that even if crevasse do close, they remain weak planes that are prone to reactivating under appropriate stress conditions. For simplicity, we restrict calving to occur along vertical planes of the glacier and assume calving occurs when crevasses penetrate through the entire glacier thickness.

Shear localization

To determine shear localization, we examine the shear stress in the ice and check for maximum shear stress at the calving front exceeding the shear strength τ_c (set arbitrarily to 130 kPa here). Empirically choosing a value of 130 kPa is sufficient for shear localization in our test cases, and we focus our analysis on the nature of the calving retreat. If the maximum shear stress exceeds the threshold of 130 kPa, we emulate an idealized calving event by assuming a 45 degree failure originating at the base of the calving front and remove the calved ice from the model domain. We then run the model forward to see the effects of tensile failure on the altered geometry. Results are insensitive to changes in the failure angle as long as the maximum shear stress exceeds the threshold for a calving event.

3.3 Model Implementation Details

3.3.1 Flow solver

We implement our model using the open source finite element solver FEniCS using mixed Taylor-Hood elements with CG2 elements for velocity and CG1 elements for pressure (Alnæs and others, 2015). We solve the incompressible flow equations (Eqn

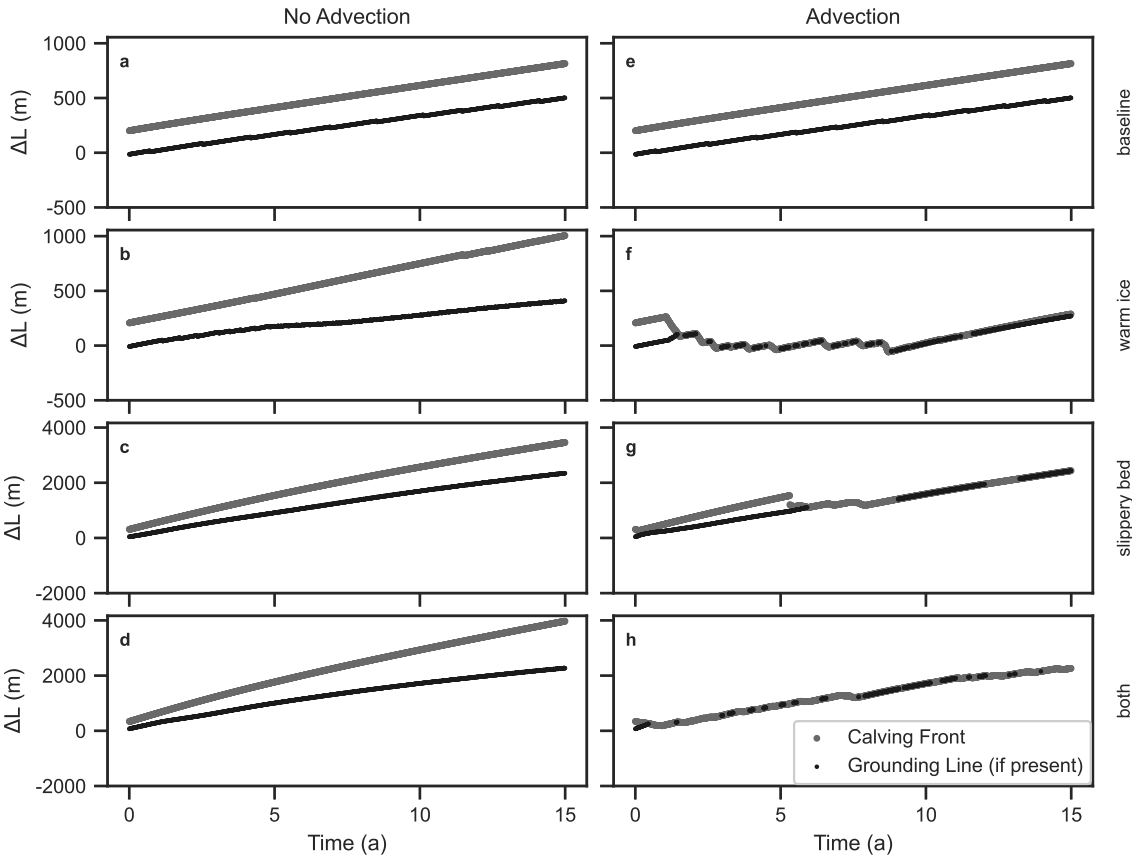

Figure 3.3: Glacier length change over time relative to initial grounding line position without advection (a-d) and with advection (e-f) (omitting shear localization) for baseline parameters (a,e), slippery bed (b,f), warm ice (c,g), and both slippery bed and warm ice (d,h). Grounding line is plotted only when the glacier terminus is floating. The inclusion of crevasse advection causes ice tongue disintegration for three of the parameter sets. The effect of advection on terminus position is most pronounced for warmer ice, where we observe retreat and then stabilization of the calving front for approximately a decade before re-advance.

(3.1)) using Picard iterations with a linear solver and calculate the acceleration term in the momentum balance using a backwards Euler step with a zero velocity initial condition (Berg and Bassis, 2020). For all simulations we use a maximum time step of 3 days and restrict to a shorter time step if necessary based on the CFL criterion with a Courant number of 0.5. Decreasing the time step does not affect results, indicating numerical convergence.

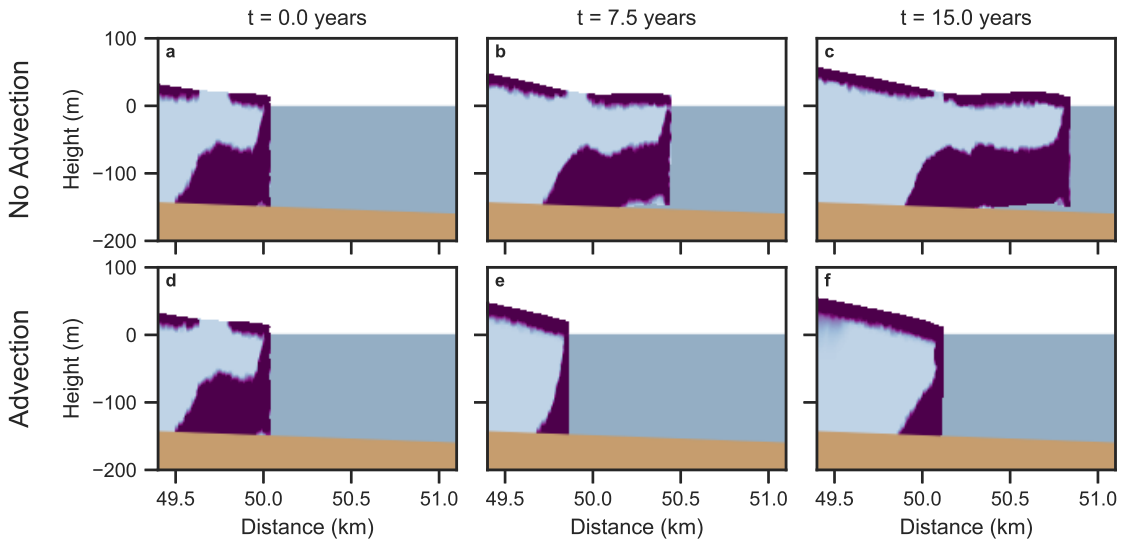

Figure 3.4: Glacier evolving in time without advection (a-c) and with advection (d-f). Warm ice parameters as given in Table 3.1. Without advection, the ice tongue grows and advances over time. Advection increases calving, leading to ice tongue disintegration followed by stabilization of calving front position for approximately a decade. At the end of simulation, the grounded calving cliff has started to re-advance.

3.3.2 Boundary forces

We implement the no penetration boundary condition on Γ_2 (Eqn (3.4)) by adding an additional force on grounded ice. This force represents the elastic properties of subglacial rock and sediment and is numerically equivalent to a penalty method. This boundary condition is given by:

$$\sigma \cdot \hat{n} = \alpha(\mathbf{r}_b - \mathbf{r}) \quad \text{on} \quad \Gamma_2. \tag{3.8}$$

The elastic force is directly proportional to the distance under the bed that the ice has penetrated, where the location of the bed is denoted by $\mathbf{r}_b$, the location of the ice is $\mathbf{r}$, and α is the elastic coefficient. We use a value of 100 $\frac{\text{kPa}}{\text{m}}$ for the elastic coefficient. Our results are insensitive to the value of α over a wide range, and our chosen value agrees broadly with measurements of the Young's modulus of glacial

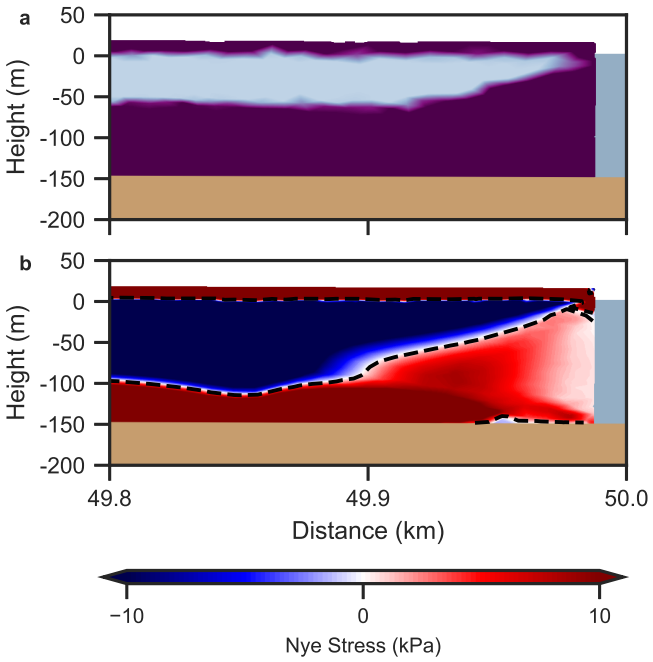

Figure 3.5: Glacier crevasses (a) and Nye stress (b) after ice tongue collapse, 2 years after start of simulation. Warm ice parameters as given in Table 1. The contour of zero Nye stress is indicated by a dashed black line, indicating regions of newly crevassed ice. Current Nye stress is insufficient for basal crevasse formation at the base of the calving front. However, basal crevasses developed when the glacier had a ice tongue are present and cause further calving.

till. Taking the Young's modulus of a loose glacial till to be 10 MPa (Bowles, 1996), our value for the elastic coefficient corresponds to a plausible glacial till thickness of 100 m (Walter and others, 2014).

For implementation of the elastic bed force and force due to water pressure (Eqn (3.5) and Eqn (3.8)), we introduce a damping term for vertical velocities to ensure that the ice displacement during flotation or rebounding from the bed is numerically stable. These damping terms are those of the form derived in Durand and others (2009), which result from a Taylor expansion in the vertical position dependence of the elastic and water pressure forces and includes dependence on the time step Δt:

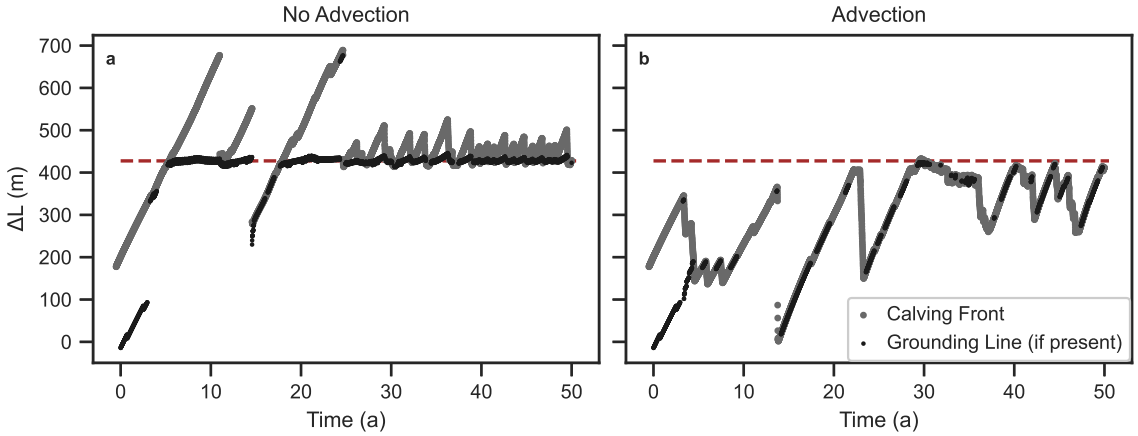

Figure 3.6: Glacier length change over time relative to initial grounding line position without advection (a) and with advection (b) (omitting shear localization) for a constant prograde bed with a Gaussian bump 250 m ahead of the glacier starting position. Brown dashed line indicates location of the sill. Baseline parameters as given in Table 3.1. Grounding line is plotted only when the glacier terminus is floating. Both tests have a transient period characterized by large calving events before settling into steady behavior after approximately 30 years. With advection, the sill strongly inhibits glacier advance, leading to a stable calving cliff. Without advection, an ice tongue forms and periodically calves, giving a stable grounding line at the sill.

$$\begin{aligned} \sigma \cdot \hat{n} &= -\rho_w g \Delta t \, (\mathbf{u} \cdot \hat{z}) \, \hat{z} \quad \text{on} \quad \Gamma_2 \\ \sigma \cdot \hat{n} &= -\alpha \Delta t \, (\mathbf{u} \cdot \hat{z}) \, \hat{z} \quad \text{on} \quad \Gamma_3. \end{aligned} \tag{3.9}$$

3.3.3 Tensile crevasses

To advect tensile crevasses in the model, we use massless tracers in a "particle-in-cell" method and store the binary crevasse field independently from the finite element mesh. Using particles to advect tracer properties limits numerical diffusion and allows us to resolve sharp changes separating regions that are crevassed from those that are not. We use LEoPart (Maljaars and others, 2020) to implement the particle-in-cell advection, an add-on to FEniCS that includes this functionality.

A set of tracers are randomly distributed throughout the domain with 32 tracers initially in each cell. At each time step, the diagnostic stress is projected to a DG1 space and then evaluated at the particle locations to determine if new crevasses form.

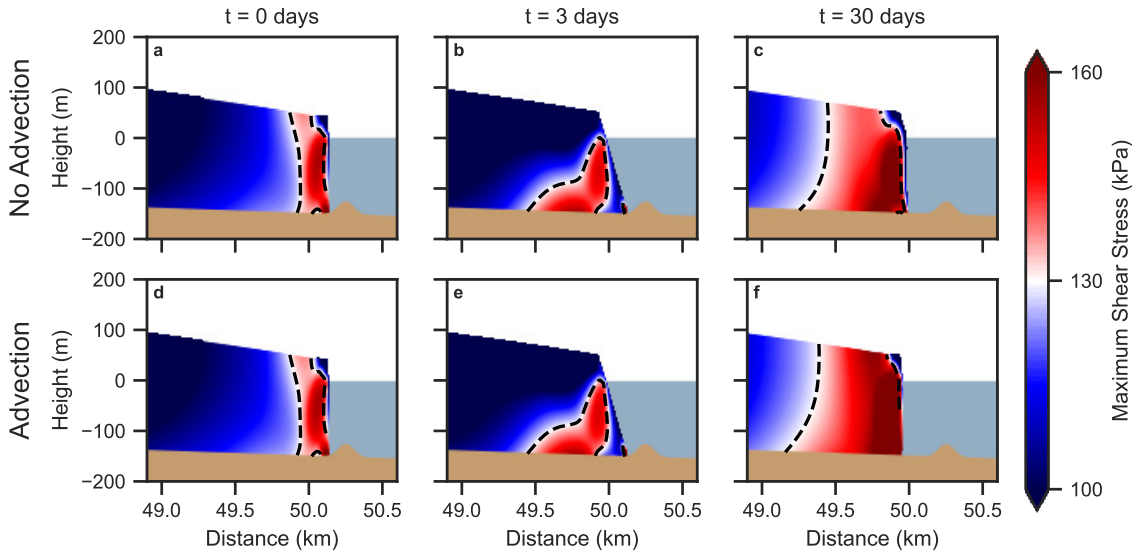

Figure 3.7: Maximum shear stress during manual shear localization test using a shear strength of 130 kPa without advection (a-c) and with advection (d-f). The contour of 130 kPa maximum shear stress is indicated by a dashed black line. Baseline parameters as given in Table 3.1. In both cases, further retreat due to tensile failure after a single shear calving event leads to an ice cliff that would calve again under high shear stress. With advection, the calving front retreats slightly further, exposing a higher cliff with larger shear stresses.

Similarly, the velocity solution on a CG2 space is evaluated at the particle locations to advect tracers.

After every time step, we analyze the stress field using a method similar to that used by (Todd and Christoffersen, 2014). We generate a contour of crevassed ice based on the binary scalar crevasse field stored on the tracers. This contour indicates where the ice transitions from crevassed to intact. In places where the contour indicates crevassed ice through the entire ice thickness, vertical calving occurs due to tensile failure and all ice downstream of the calving event is removed. After a calving event and subsequent remeshing, tracers are added to the domain randomly to maintain a minimum of 32 tracers per cell and initialized by interpolating existing tracers. Figure 3.2b shows a snapshot of the crevasse field during a modeled calving event with tensile crevasse advection and the location of calving based on our criteria.

In our implementation, calved ice "vanishes" and does not provide any back stress after detachment from the glacier, neglecting the effect of mélange on future calving.

3.3.4 Initial conditions

We initialize the bed and ice surface to a constant prograde slope of 0.01 and constant thickness of 200 m from the ice divide boundary to the terminus at 50 km, roughly consistent with geometry of Svalbard outlet glaciers (Dunse and others, 2012). From the initial ice configuration we run the model with the calving front held fixed at its initial location until the ice relaxes to a steady state (2500 a). Once the glacier has reached steady state, we allow the ice to flow unconstrained an additional 0.5 years to ensure complete relaxation and then allow calving using the Nye zero stress criterion. We do these experiments with and without advection of crevasses and start simulations with no crevasses initially present in the glacier.

3.3.5 Meshing

We use the external remeshing package Gmsh (Geuzaine and Remacle, 2009) for remeshing of the domain. Using Gmsh, we have precise control over the meshing process and break the glacier into high resolution and low resolution subdomains. Dividing the glacier into high resolution and low resolution regions allows us to simulate the entire glacier and maintain the ice divide boundary condition (Eqn (3.4)) upstream while avoiding excessive computation time. We use an initial mesh size of 10 m in the high resolution region and a mesh size of 100 m in the low resolution region, with the high resolution region starting five ice thicknesses upstream of the grounding line. Model results are insensitive to changes in the low resolution mesh size and converged with high resolution mesh size such that sizes smaller than 10 m do not significantly change results. We remesh after every calving event or when the

ratio of minimum to maximum cell radii drops below a threshold of 0.1 according to the built in FEniCS mesh quality class.

3.4 Suite of Tests

To test the effects of crevasse advection on calving behavior in different environments, we ran the model on a set of parameters with different ice temperatures and sliding coefficients. These parameter sets are listed in Table 3.1 in four different combinations: baseline, warm ice, slippery bed, and warm ice and slippery bed. A constant surface mass balance of 0.25 m/a is applied in all cases, a moderate value for the Austfonna ice cap (Schuler and others, 2007).

3.4.1 Ice temperature

We use a moderate temperature of $-10°\mathrm{C}$ as our baseline temperature, roughly corresponding to near surface temperatures on Jackobshavn Isbræ(Iken and others, 1993; Lüthi and others, 2002) and modeled ice temperatures of the Austfonna ice cap (Østby and others, 2013). To investigate the case of warmer ice we use a temperature of $-2°\mathrm{C}$, which agrees with borehole observations of warmer Greenland glaciers (Harrington and others, 2015) and modeled melt season temperatures at Austfonna (Harrington and others, 2015). The Glen's flow law coefficient B was taken for each temperature from the values given by Hooke (2005).

3.4.2 Sliding coefficient

We use a baseline sliding coefficient of $7.6 \times 10^6\,\mathrm{Pa\,m^{-\frac{1}{3}}\,s^{\frac{1}{3}}}$, which is identical to the coefficient used for the modified Weertman sliding law in the Marine Ice Sheet Intercomparison Project (Pattyn and others, 2012). Because this is a fairly high sliding coefficient, we halve the coefficient to see the effects of a more slippery bed.

3.4.3 Bed slope

In addition to the ice temperature and sliding coefficient tests on a constant prograde slope, we also perform tests on a prograde bed with an idealized sill to investigate the combination of varying bed topography and advection on calving behavior. In this case, we superimpose a Gaussian bump with amplitude 25 m and standard deviation 50 m on the constant prograde bed 250 m ahead of the initial calving front.

3.5 Results

3.5.1 Effect of crevasse advection on calving

Constant slope prograde bed

We first examined the effect of crevasse advection on terminus position using a prograde bed without a sill and without shear localization. Figure 3.2 and shows snapshots illustrating initial ice tongue advance with and without advection on a slippery bed. Without advection (Figure 3.2a), bending near the calving front results in a compressive stress at the grounding line that prevents basal crevasse formation. However, with advection (Figure 3.2b), basal crevasses that initiate just upstream of the grounding line advect past the grounding line, resulting in a crevassed region that penetrates the entire thickness 300 m upstream from the calving front. This effect is shown over time in Animation S1. Advection causes increased calving frequency and decreased glacier length relative to when advection is omitted.

The cumulative effect of the increased calving frequency is illustrated in Figure 3.3, which shows the change in glacier length over time relative to initial grounding line position for the suite of scenarios. In the baseline parameter tests (Figures 3.3a,e), advection makes little difference to glacier terminus position. However, when

we decrease the sliding coefficient (more slippery bed) or increase ice temperature (warmer ice), we see advection has a larger effect on terminus position. For example, in all tests that have warmer ice or a lower sliding coefficient (Figures 3.3f-h), the ice tongue disintegrates, resulting in a grounded calving cliff. This is a consequence of the enhanced deformation of the calving front associated with these conditions, widening the region where the Nye zero stress is positive within the glacier. The warmer ice and slippery bed conditions are representative of many Greenland glaciers that only rarely form permanent floating tongues.

Crevasses formed upstream of the grounding line when the glacier had an ice tongue persist after ice tongue disintegration, resulting in transient behavior as these crevasses advect through the system. For example, Figure 3.5 shows crevasses and the Nye stress after ice tongue disintegration for warm ice. The Nye stress is insufficient to form sufficient basal crevasses near the calving front. However, with advection, existing crevasses take time to move through the domain resulting in a transient that can last a few years to a decade.

Crucially, the contribution of advection is most pronounced for our test with warm ice (Figure 3.3f, Animation S2). Glacier retreat continues after ice tongue disintegration and results in a stable grounded calving front position upstream from the initial calving front for approximately a decade before the glacier starts re-advance. This temporary retreat followed by re-advance is observed in the other tests but is shorter: approximately two years with a slippery bed (Animation S1) and under a year for warm ice with a slippery bed. In the slippery bed simulations, increased deformation rapidly exports transient basal crevasses away from the grounding line. In the warm ice with a slippery bed case, the short ice tongue disintegrates quickly and is not able to form basal crevasses near the grounding line. These results hint

that glacier calving behavior is not solely a consequence of immediate forcing and suggests glacier advance or retreat could be dependent on earlier conditions.

Surprisingly, in no case do we observe sustained glacier retreat regardless of ice temperature or sliding coefficient. Instead, glaciers either advance or temporarily retreat to a terminus position upstream before re-advancing. However, this may be a consequence of the constant prograde bed.

Stabilizing behavior of sill

Because many glaciers stabilize on sills near the terminus, we performed simulations using our baseline parameter set with a bump in the bed. In tests with and without advection, when the ice tongue is forced over the sill, high bending stresses at the grounding line cause a large calving event that removes the ice tongue. The newly formed grounded ice cliff advances again towards the sill. After a few large calving events, both tests achieve steady behavior after approximately 30 years. Glacier evolution for a total of 50 years is shown in Animation S3.

Without advection, Figure 3.6 shows that the glacier advances over the sill and forms a short ice tongue. The tongue periodically disintegrates from increasing deformation at the top of the calving front as the ice tongue advances. Thus, even in the absence of advection, bed geometry has a strong effect on glacier advance. However, without advection, the glacier retains a short floating ice tongue that may provide some protection against perturbations in ocean forcing.

In contrast, when advection is included, Figure 3.6 shows that the sill strongly inhibits advance and the glacier forms a stable calving cliff at the location of the sill. As the glacier advances over the bump in the bed, a higher cliff and the concave bed shape increase stresses. Advected crevasses caused by these higher stresses inhibit advance over the sill. We also observe brief periods where the glacier temporarily

retreats to the base of the sill before re-advancing at approximately 37 years, 42 years, and 47 years. This behavior is caused by slowly advecting surface crevasses at the top of the calving cliff that eventually meet with basal crevasses and cause a more significant calving event.

The resulting calving front is qualitatively similar to Store Glacier, which terminates at a bump in the bed (Todd and Christoffersen, 2014). Store glacier exhibits ice front advance and retreat coinciding with the presence of seasonal ice mélange (Howat and others, 2010), with our advection results showing behavior similar to Store glacier in the absence of additional mélange back stress. In our simulations, glaciers advance on a prograde bed until they reach a bump in the bed where they can stabilize. This is analogous to the behavior of most stable glaciers that remain perched on sills, but our model still fails to reproduce sustained retreat.

3.5.2 Effect of shear localization

Tensile crevasse advection is sufficient in our model to cause temporary glacier retreat on a prograde bed and grounded calving cliffs on a sill. However, we also investigate the effects of idealized shear localization on subsequent calving behavior. Here we examine the onset of tensile failure after a single shear localization event. We focus on a recently retreated grounded calving cliff in our advection experiment with a sill, which we expect to have higher shear stress at the calving front.

Starting with an initial geometry immediately after the glacier retreat corresponding to approximately 37 years elapsed in our previous test, the shear stress exceeds our chosen threshold of 130 kPa. Figure 3.7 shows results with and without crevasse advection as the glacier evolves over the next 30 days after the initial shear calving event. In both cases, buoyant stresses cause cascading tensile failure events. Glacier retreat continues until a second ice cliff with high shear stress is reached.

Advection slightly increases the magnitude of retreat, leading to higher shear stresses in the new ice cliff when compared to the case without advection. However, in both cases the shear stress increases after rapid tensile failure, indicating catastrophic retreat regardless of crevasse advection. Therefore, the coupling of tensile failure and shear localization predicts catastrophic retreat where tensile failure and crevasse advection does not. However, in this test our threshold for shear failure is low and we don't anticipate glaciers with such low shear stresses to disintegrate.

3.6 Discussion

Our results show that tensile failure and shear localization contribute to significantly different styles of calving behavior. In our suite of tests, advection of tensile crevasses results in advancing glaciers or stabilization on a sill. However, we do not observe sustained retreat in any of these cases. One possible reason for the minimal observed retreat in our model is the omission of submarine melt. Submarine melt rates vary over a wide range. For example, estimated values in Hansbreen, Svalbard span the range from 0-15 m/week (De Andrés and others, 2018), which would strongly contribute to total mass loss.

Furthermore, calving rates for Svalbard glaciers are strongly dependent on ocean temperature (Luckman and others, 2015) and previous modeling has demonstrated that relatively small melt rates can promote calving (Ma and Bassis, 2019)—an effect that could be magnified with the inclusion of tensile crevasse advection. A melt profile focused at the grounding line reduces glacier thickness and promotes a buoyant transition. This could increase the contribution of tensile crevasse advection to calving rates given that we see the deepest advected crevasses near the grounding line as the ice transitions to flotation. Nonetheless, our results suggest that, with the

exception of significantly thicker glaciers where shear localization may play a role, internal stresses within the glaciers alone are insufficient to trigger retreat due to calving. Instead, retreat is more likely driven by ocean melt along the calving front or water filling surface crevasses and allowing deeper penetration depths.

In contrast, shear localization and mixed-mode failure has a much stronger contribution to rapid, unstable retreat. In our model, when a piece of the glacier is removed via failure due to shear localization, a series of buoyant calving events quickly expose a second, higher calving cliff. This higher cliff has higher shear stress and the continuing cycle of a shear event followed by buoyant calving leads to complete disintegration. Because the process is rapid, it is not dependent on the advection of crevasses and is purely driven by the interaction between the two failure modes.

However, there are sources of stabilization to the catastrophic failure that are not accounted for in our model. For example, we do not include coupling between crevasses and the ice rheology. Coupling of crevasses with the rheology may decrease cliff heights, reducing calving from shear localization and the potential for catastrophic collapse. However, a different rheology could affect tensile failure as well. If viscosity decreases as ice becomes crevassed, ice may fail more easily under tensile failure. This could increase the effect of tensile crevasse advection on calving behavior.

Another possible contributor to stabilization is backstress due to calved mélange rather than instantaneously removing all calved ice from the model domain. Back stress from mélange has been shown to have significant effects on calving behavior (Todd and Christoffersen, 2014; Joughin and others, 2012). For a rapidly retreating grounded ice cliff, the rapid buildup of mélange would provide significant stabilizing stress and potentially stop collapse. Additionally, the catastrophic collapse observed

in our model is contingent upon our choice of glacier shear strength. Because shear stress increases with grounded ice cliff height (Bassis and Walker, 2012), this collapse mechanism is not important for small outlet glaciers such as Store glacier, but could be important for larger glaciers such as Thwaites Glacier or Pine Island Glacier.

Specifying a more precise threshold for shear localization and improving understanding of mixed-mode failure is crucial for future modeling of glacier collapse. However, advection, which is easily included in existing models, also appears to play an important role in controlling glacier behavior. This is especially important because phases of retreat and advance are not necessarily instantaneously connected with climate forcing. Instead, we anticipate a response time comparable to the time it takes crevasses to advect through the domain. This may aid in explaining some of the confusion in attributing glacier retreat to atmospheric or oceanic forcing.

3.7 Conclusion

Our results show that when tensile failure is the only mode of failure and advection is omitted, glaciers continuously advance. Including tensile crevasse advection in a two dimensional flowline calving model reduces the overall rate of advance by increasing calving and also leads to temporary glacier retreat. Because crevassed ice is allowed to persist over time, crevasses formed near the grounding line of the glacier advect and cause ice tongues to periodically calve, exposing a grounded cliff. This effect is more pronounced with warmer ice. Advection also enhances the importance of basal topography. Crevasse memory contributes strongly to calving events as a glacier approaches a sill and prevents further advance, leading to a stable ice cliff rather than a transient ice tongue.

Although crevasse advection does increase the contribution of calving to glacier

mass loss, it does not cause catastrophic collapse in the absence of additional driving factors such as shear calving. For a grounded terminus, we conduct some idealized tests on the consequence of a shear calving event and show that the combination of shear localization and tensile failure can cause catastrophic retreat.

Given that basal crevasses dominate the advection related effects in our study, the importance of ocean forcing may increase when coupled with crevasse advection. Small increases in melt to a previously stable calving front position could drive a glacier into a regime of catastrophic retreat initiated by shear localization. Without advection, less calving and a buttressing ice tongue would necessitate a more dramatic change in ocean forcing to catalyze retreat. Our study shows that tensile crevasse advection can play a significant role of calving behavior and shear localization could be a key contributor to catastrophic collapse. Future calving models should take care to include a mechanism for advection and multiple modes of calving whenever possible.

CHAPTER IV

Collapse in Mixed Mode Calving Model Highly Sensitive to Shear Strength

This chapter is a draft manuscript currently in preparation for publication.

4.1 Introduction

Models of the iceberg calving process remain a large source of uncertainty in mass loss from ice sheets and their corresponding contribution to sea level projections (Stocker and others, 2013; Pörtner and others, 2019; Pattyn and Morlighem, 2020). Developing improved models that can better reproduce the diversity of calving behaviors and physical drivers of the calving process is essential to inform large scale ice sheet and glacier models.

The high source of mass loss uncertainty from calving is exacerbated by debate regarding the importance of the marine ice cliff instability, originally proposed by Bassis and Walker (2012). The marine ice cliff instability starts when ice cliffs reach the critical height where shear stress overcomes the strength of ice and calving occurs. This exposes a higher ice cliff and because the shear stress scales linearly with the height of the cliff, leads to catastrophic retreat. Although such an instability has never been directly observed in modern observations, paleo records provide hints and

clues that it might have occurred in the past. For example, marine ice cliff instability has been implicated in Heinrich events—massive armadas of icebergs episodically discharged from the Laurentide Ice Sheet (Bassis and others, 2017). Similarly, iceberg scour marks in the sea floor have been used to infer that the ice thickness in the Amundsen Sea Embayment portion of West Antarctica rarely exceeded the critical height (Wise and others, 2017).

However, because a marine ice cliff instability type collapse has never been directly observed in modern ice sheets, the hypothesis remains controversial with disagreement on the necessity of including it in ice sheet models (Edwards and others, 2021; DeConto and others, 2021). One study done by Bassis and others (2021) implicitly includes shear localization via a complex ice rheology, albeit at high computational cost. However, the number of calving models running at longer temporal scales that explicitly include shear localization as a failure mechanism is limited.

Although too computationally expensive to be used for predictions at the ice sheet scale, full Stokes models of glaciers are a valuable tool to examine the physical drivers of glacier advance and retreat and can be designed to run on timescales of years to decades. Previous full Stokes models have considered the effects of damage advection on calving behavior (Pralong and Funk, 2005; Borstad and others, 2012; Duddu and others, 2013; Krug and others, 2014; Jiménez and others, 2017), using damage as a continuous variable to broadly track regions of crevassed ice. Other models have included additional effects such as submarine melt (Todd and Christoffersen, 2014; Todd and others, 2019; Ma and Bassis, 2019) or mixed mode failure Crawford and others (2021). However, none have studied the simultaneous interplay between crevasse advection, submarine melt, and mixed mode failure.

In this work, we improve upon a previously developed model presented in Chapter

III that was designed to probe the effects of crevasse advection on tensile failure behavior. Given that submarine melt accounts for a high percentage of mass discharge from glaciers and ice sheets (van den Broeke and others, 2009; Enderlin and Howat, 2013) and even small amounts of melt can increase calving (Ma and Bassis, 2019), we examine the effect of submarine melt in the model. Second, and more importantly, we add shear localization into the model. The inclusion of both tensile failure, shear localization, and crevasse advection allows us to gain a more complete picture of the calving process due to a wider range of mechanisms. Novel in our model is the ability for calving events due to a combination of different fracture origins, where part of the fracture occurs due to shear localization and another part occurs to tensile failure.

4.2 Model Description

Our model builds on Chapter III. Below we describe the failure mechanisms we include in our model, along with our implementation of submarine melt.

4.2.1 Tensile failure

We use the 'Nye zero stress' model, which assume tensile failure occurs when the greatest effective principle stress σ_{Nye} is greater than the tensile strength of ice T_0. This is an appropriate approximation for closely spaced crevasses, typical of most outlet glaciers. We, however, allow for a general nonzero strength of ice T_0 more realistic for ice. The greatest effective principle stress is defined as the sum of the greatest principle stress σ_1 and the water pressure at a given depth:

$$\sigma_{\text{Nye}} = \sigma_1 + \rho_w g z_w > T_0, \tag{4.1}$$

where ρ_w is the density of water, g is the acceleration due to gravity, and z_w is

the depth under water. This criterion assumes that pressure from ocean water filling crevasses contributes to the stress field. Tensile failure occurs along the plane corresponding to the greatest principle stress that causes the failure, which is approximately vertical in the cases considered here.

The strength of ice under tensile failure as a function of the critical stress intensity factor of mode-I crack propagation K_{IC}, and c, where $2c$ is the length of pre-existing starter cracks is given byAshby and Hallam (Née Cooksley) (1986) as:

$$T_0 = \frac{K_{Ic}}{(\pi c)^{1/2}}. \tag{4.2}$$

This form of the tensile strength is useful because the shear strength can be consistently specified using the same set of material parameters.

4.2.2 General Coulomb failure

The criteria for shear localization follows (Schulson, 2001; Jaeger and others, 2009). Shear localization along a given plane will occur if the shear stress along that plane exceeds the shear strength of the ice and the internal friction of the ice. This criterion is expressed as:

$$|\tau| > S_0 + \mu\sigma, \tag{4.3}$$

where $|\tau|$ is the magnitude of the shear stress along a given plane, S_0 is the shear strength of ice, μ is the coefficient of internal friction, and σ is the normal stress acting along the same plane.

As shown by Jaeger and others (2009), in two dimensions Equation 4.3 can be rewritten as:

$$\left(1 + \mu^2\right)^{\frac{1}{2}} \tau_m > S_0 + \mu\sigma_m, \tag{4.4}$$

where τ_m is the maximum shear stress and σ_m is the two-dimensional mean stress. τ_m and σ_m can be expressed in terms of σ_1, the greatest principle stress, and σ_2, the smallest principle stress, as:

$$\begin{aligned} \tau_m &= \frac{1}{2}\left(\sigma_1 - \sigma_2\right) \\ \sigma_m &= \frac{1}{2}\left(\sigma_1 + \sigma_2\right). \end{aligned} \tag{4.5}$$

In addition to exceeding the necessary stress threshold for failure, an additional constraint is placed upon the Coulomb failure criterion. First, we define the confinement ratio as the ratio of the least compressive to most compressive principle stress:

$$R_{21} = \frac{\sigma_1}{\sigma_2}. \tag{4.6}$$

For confinement ratios greater than a critical ratio R_{21c} given by Renshaw and Schulson (2001) as:

$$R_{21c} = \frac{1-\mu}{1+\mu}, \tag{4.7}$$

brittle failure transitions from shear localization to a failure model called plastic faulting by Schulson (2002) and has been discussed recently in the context of ice failure and cliff instability by Clerc and others (2019). Thus, the Coulomb failure criterion only allows for failure at confinement ratios less than the critical ratio.

Renshaw and Schulson (2001) gives the equation for the critical stress leading to failure, which is equal to the shear strength S_0:

$$S_0 = \frac{2K_{Ic}}{c^{1/2}\left[\left(1+\left(1-\mu\frac{1+R_{21}}{1-R_{21}}\right)^{2/3}\right)^{1/2}-1\right]\left(1+3\mu^2\alpha^2\left(1-R_{21}\right)^2\right)^{1/2}}, \tag{4.8}$$

where α is the aspect ratio of the columns of ice spaced by comb cracks during Coulomb failure.

The angle of shear fault formation θ due to Coulomb failure relative to the principle axis associated with the most compressive principle stress is given by Jaeger and others (2009) and can be calculated using:

$$\mu = \tan\phi, \tag{4.9}$$

and:

$$\theta = \frac{\pi}{4} - \frac{\phi}{2}. \tag{4.10}$$

Once large secondary cracks have formed via the above failure mechanism, they are considered permanent and can reactivate under the appropriate stress conditions. Following the process outlined by Moore and others (2010) and where only friction inhibits further faulting, this condition is:

$$\frac{(\sigma_2 + \rho_w g z_w)}{(\sigma_1 + \rho_w g z_w)} = \frac{(1 + \mu\cot\gamma)}{(1 - \mu\tan\gamma)}, \tag{4.11}$$

where γ is the angle between the existing fracture orientation and σ_2.

However, due to limitations with the binary and continuous nature of our crevasse tracking method presented in Chapter III, we do not track the fault angle of individual fractures over time. Therefore, we restrict our implementation of crevasse advection to tensile failure and assume that shear localization must always satisfy the stress criteria in Equation 4.8. This will lead to an underestimate of calving due to shear localization for our model.

4.2.3 Coulomb failure with zero internal friction

The internal friction of ice can vary widely with temperature and sliding velocity from close to zero to close to one (Kennedy and others, 2000; Schulson, 2001). Be-

cause of the uncertainty associated with choosing a friction coefficient, we remove it from our analysis by setting it to zero for the remainder of this study and focus our analysis on the strength of ice. However, increasing internal friction would qualitatively have a similar effect as increasing shear strength while keeping tensile strength constant.

If the coefficient of internal friction μ is zero, Equation 4.4 simplifies to:

$$\tau_m > S_0. \tag{4.12}$$

In the absence of internal friction, Equation 4.4 simplifies to the straightforward assertion that the maximum shear stress must exceed the shear strength of ice for failure to occur. In two dimensions, this is identical to the von Mises yield criterion for ductile materials. Figure 4.1 shows a general failure envelope with zero internal friction for an arbitrary tensile strength T_0 and shear strength S_0. Three regimes exist: tensile failure due to high extensional stress, shear failure due to high shear from compressive stress, or no failure from compressive stress.

Setting internal friction to zero in Equation 4.8 gives a simplified form of the shear strength of ice:

$$S_0 = \frac{2K_{Ic}}{c^{1/2}}. \tag{4.13}$$

Using Equation 4.2 and Equation 4.13, the tensile strength and shear strength of ice can be specified consistently using only the critical stress intensity factor of mode-I crack propagation and the length of pre-existing starter cracks. Figure 4.2 shows both tensile strength and shear strength as a function of starter flaw size c given a critical stress intensity factor of 0.05 M Pa $\mathrm{m}^{\frac{1}{2}}$ as given in Table 4.1.

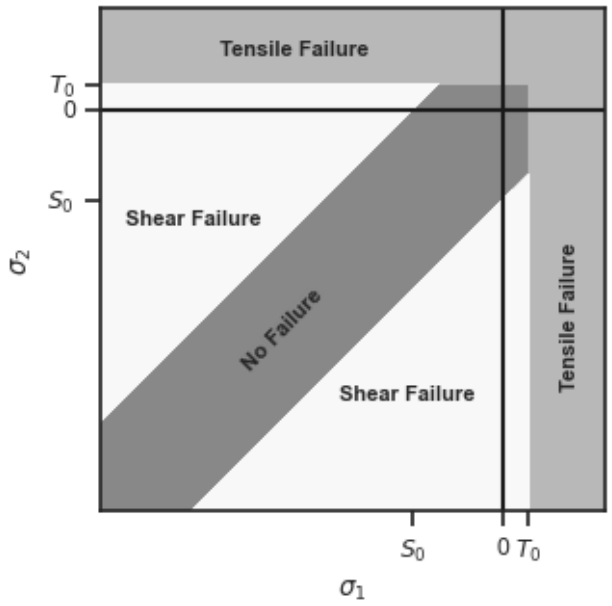

Figure 4.1: General calving failure envelope with tensile strength of T_0, shear strength of S_0, and zero internal friction. Shading and labels indicate regions of tensile failure, shear localization, and no failure.

Additionally, when assuming zero internal friction, the critical confinement ratio given in Equation 4.7 is equal to one and therefore failure will never transition to plastic faulting. Lastly, based on Equation 4.9 and Equation 4.10, zero internal friction gives a constant fault angle of 45 degrees.

4.2.4 Submarine melt

In this study, we also examine the interplay between submarine melt and calving from mixed mode failure. In our implementation, submarine melt is applied to the exterior of the glacier at all points underwater and downstream of the grounding line. For this purpose, we define the grounding line to be the furthest downstream location where ice is in contact with the bed. Therefore, we do not include any melt due to ocean water intrusion at the bed or due to frictional heating between the glacier and the bed.

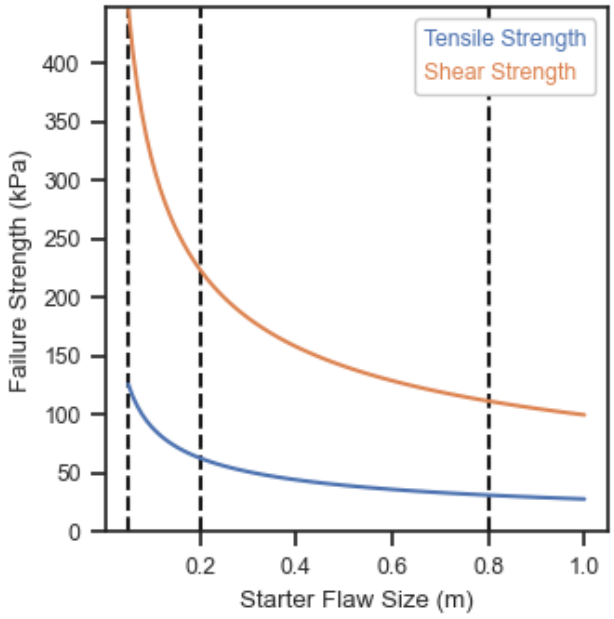

Figure 4.2: Failure strengths as a function of starter flaw size for a constant critical stress intensity factor. Dashed vertical lines indicate starter flaw sizes used to select the approximate failure strengths in this study. Chosen starter flaw sizes are 0.05 m, 0.2 m, and 0.8 m.

Following the study of Ma and Bassis (2019), we use a parabolic melt rate of the form:

$$\dot{m}(z) = 6\bar{\dot{m}}\frac{z}{D}\left(1 - \frac{z}{D}\right), \tag{4.14}$$

where $\bar{\dot{m}}$ is the specified depth-averaged melt rate, D is the water depth, and z is the vertical position relative to the bed. Melt undercutting due to submarine melt maximized between the ocean surface and the bed has been observed (Rignot and others, 2015) and modeled (Sciascia and others, 2013; Slater and others, 2017). Previous work by Ma and Bassis (2019) has shown that a parabolic melt profile has a moderate effect on calving behavior. Lastly, using a parabolic melt profile has model implementation advantages, avoiding numerical issues that arise from applying melt directly at the base of a calving cliff.

Table 4.1: List of constant parameters used in model tests.

Parameter	Value
Basal Friction Coefficient	$7.6 \times 10^6\,\mathrm{Pa} \cdot \mathrm{m}^{-\frac{1}{2}} \cdot \mathrm{s}^{\frac{1}{3}}$
Ice Temperature	$-2°\mathrm{C}$
Surface Mass Balance	0.25 m/a
Average Submarine Melt	0.1 m/day
Critical Stress Intensity Factor	$0.05\ \mathrm{M\ Pa\ m}^{\frac{1}{2}}$

4.3 Model Implementation and Tests

The flow, tensile failure, and crevasse advection parts of the model are implemented in FEniCS (Alnæs and others, 2015) and LEoPart (Maljaars and others, 2020) identical to the study presented in Chapter III. We use a modified Weertman sliding law and basal friction coefficient identical to the coefficient used in the marine ice sheet intercomparison project (Pattyn and others, 2012). For all tests, we use constant values for basal friction coefficient, ice temperature, surface mass balance, and submarine melt as given in Table 4.1. Ice temperature is chosen to be consistent with temperatures of tidewater glaciers in West Greenland (Harrington and others, 2015). Submarine melt can vary seasonally and spatially over a wide range from centimeter to meters per day. Our chosen average submarine melt of 0.1 m/day is on the higher end for cold tidewater glaciers in Antarctica and on the lower end of estimates for warmer Greenland glaciers (Truffer and Motyka, 2016).

Meshing is also handled in an identical fashion using Gmsh (Geuzaine and Remacle, 2009), with 10 m mesh resolution close to the grounding line and 100 m upstream. Results are converged at these resolutions are not affected significantly by altering either mesh size. Maximum time step is set to 3 days and restricted to a shorter time step based on the CFL criterion with a Courant number of 0.5. Model results are insensitive to shorter time step sizes.

For shear localization, at each time step local extrema of maximum shear stress

are identified on the exterior of the glacier. These local extrema are the possible starting points of shear faults. For each local extrema, conjugate fault planes (at 45 degrees for zero internal friction) are traced out using a step distance equal to the high resolution mesh size. Tracing the fault plane continues until the maximum shear stress is too low to exceed the shear strength or the fault intersects with the glacier boundary.

If a shear fault intersects a region of ice that either exceeds the tensile failure criteria or has advected tensile crevasses, the fault will preferentially propagate vertically rather than along the 45 degrees shear direction. In this manner, we trace out faults that are truly mixed mode and are due to more than one brittle failure mechanism. As in Chapter III, if any calving event occurs, the downstream ice is removed instantaneously.

4.3.1 Model geometries

We perform a total of three suites of tests. First, we examined a constant prograde bed with a slope of 0.01, an initial length of 50 km, and a constant thickness of 200 m. This geometry is identical to that used in Chapter III and is in agreement with the basic geometry of Svalbard outlet glaciers (Dunse and others, 2012). Surface mass balance of 0.25 m/a is uniformly applied to the glacier surface and the model is run with the calving front held constant until the glacier reaches steady state with a vertical calving front. After steady state is reached (after $\sim$2500 a), calving is turned on and the glacier is allowed to evolve normally in time. The second set of tests is identical except that we include a component of mass balance due to submarine melting on the calving face.

Lastly, we also super-imposed a Gaussian bump, designed to represent a proglacial sill to examine the effects of a sill on glacier behavior. This bump has an

amplitude of 25 m and a standard deviation of 50 m and is placed 250 m ahead of the steady state calving front.

4.3.2 Role of tensile and shear strength in determining behavior

To explore the effect of mixed mode failure model over a range of possible yield strengths, we varied two parameters: the tensile strength and shear strength of ice. In theory, these can be specified simultaneously using the size of pre-existing starter cracks and the critical stress intensity factor for mode-I crack propagation. However, the actual tensile and shear strengths depend on the initial orientation of pre-existing fractures and may not necessarily be optimally oriented. To explore this possibility, we varied both tensile and shear strengths independently to sweep out a larger area in the failure envelope.

For each suite of simulations, we ran the model with a variety of different ice strengths. First, we calculated tensile strengths and shear strengths using starter flaw sizes c of 0.05 m, 0.2 m, and 0.8 m, which are indicated by vertical dashed lines in Figure 4.2. This gives approximate tensile strengths of 30 kPa, 60 kPa, and 125 kPa and approximate shear strengths of 100 kPa, 225 kPa, and 450 kPa. However, in addition to testing the strength combinations derived from the same starter flaw sizes, we ran all possible combinations of tensile strength and shear strength to more fully understand the effect of varying yield strengths on calving behavior. We also added 0 kPa tensile strength tests to examine the limit of the original Nye zero stress criterion.

4.4 Results

4.4.1 Sharp thresholds in shear strength predict retreat

Figure 4.3 shows the time evolution of calving front location over 10 years of simulation for 125 kPa tensile strength with varying shear strengths and 450 kPa shear strength with varying tensile strengths. If tensile strength is held constant, varying shear strength leads to sharp transitions between types of calving behavior. At the lowest shear strength, rapid catastrophic collapse occurs at the beginning of simulation. At a higher shear strength of 225 kPa, a large initial calving event occurs, but the glacier is able to stabilize and begins to re-advance. With a shear strength of 450 kPa, nearly all calving is suppressed and the glacier constantly advances.

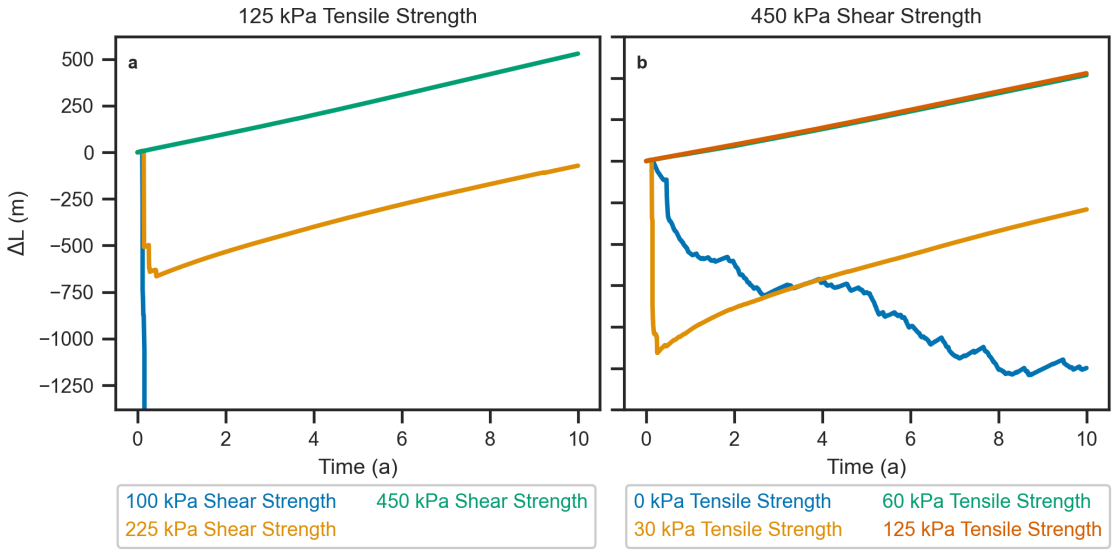

Figure 4.3: (a) Time evolution of calving front position for tests with 125 kPa tensile strength and no submarine melt. Results shown for tests with different shear strengths of 100 kPa, 225 kPa, and 450 kPa. The 100 kPa shear strength test rapidly collapses, 225 kPa has a rapid 600 m initial retreat follow by steady advance, and 450 kPa advances without any significant calving. This shows a high sensitivity to strength strength, with lower shear strengths predicting rapid collapse. (b) Time evolution of calving front position for tests with 450 kPa shear strength and no submarine melt. Results shown for tests with different tensile strengths of 0 kPa, 30 kPa, 60 kPa, and 125 kPa. Although the 30 kPa tensile strength test has a rapid 1 km initial retreat, it quickly readvances without further calving. Over 10 years, lower tensile strength predicts a lower average calving front advance rate, with negligible difference between 60 kPa and 125 kPa.

In contrast, Figure 4.3b shows that holding shear strength constant and varying tensile strength leads to smaller changes in calving behavior. With zero tensile strength, a gradual retreat of approximately 1 km occurs over the 10 year time period. A tensile strength of 30 kPa leads to a large initial calving event instead of a series of smaller events, but the glacier quickly begins to re-advance. Larger tensile strengths of 60 kPa and 125 kPa suppress nearly all calving.

Figure 4.4 shows the average calving front advance rate over 10 years of simulation for different tensile strengths and shear yield strengths. On average, as both tensile strength and shear strength are increased, there is an increase in the calving front advance rate. Varying tensile strength at high shear strengths shifts glacier behavior between slow advance and slow retreat. The glacier achieves a positive average advance rate with tensile strength greater than 60 kPa and and shear strength greater than 225 kPa. This is a clear reflection that as failure strengths increase, calving flux decreases because the glacier is less likely to fail.

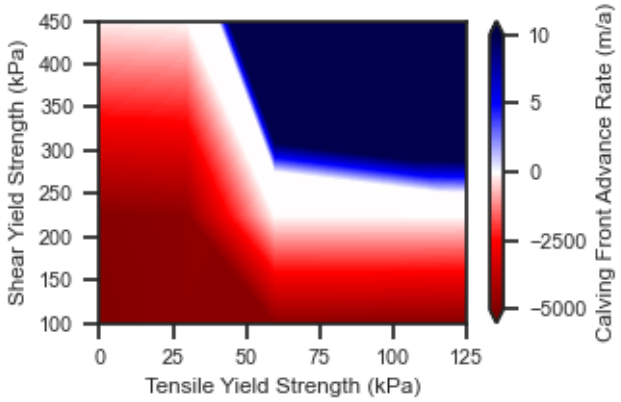

Figure 4.4: Average calving front advance rate over 10 years with varying tensile strengths and shear strengths for prograde bed without submarine melt. Higher tensile strengths cause higher advance rates and shear strengths below approximately 225 kPa cause rapid collapse.

However, at lower shear strengths, the calving behavior undergoes an abrupt tran-

sition to what could be deemed a marine ice cliff instability behavior. The glacier first slowly retreats through incremental tensile failure events. Eventually, either the ice cliff reaches sufficient height that shear localization occurs, detaching a large aerial berg, or basal tensile crevasse accumulate and contribute to an underwater calving event as shown in Figure 4.5b. This is followed by further calving events caused by changing stresses from a buoyancy adjustment (Figure 4.5c). This process continues until the glacier fully collapses. Qualitatively, this is identical to the behavior observed by Bassis and others (2021) with a different approach to modeling mixed mode failure. Catastrophic collapse is not guaranteed at low shear strengths, but a shear strength less than approximately 225 kPa appears to be a prerequisite for this behavior. Slow rather than catastrophic retreat for intermediate tensile strengths and low shear strengths indicates that varying tensile strength at low shear strengths could affect the occurrence of catastrophic collapse.

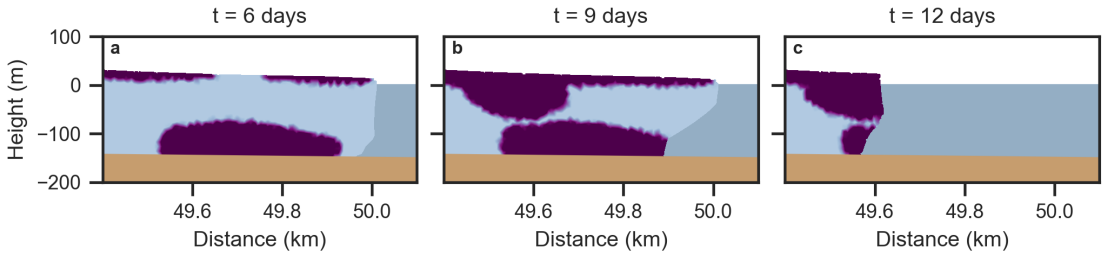

Figure 4.5: Time evolution over three time steps on constant prograde bed with submarine melt, with 225 kPa shear strength and 30 kPa tensile strength. Purple indicates areas with advected tensile crevasses. (a) Small initial calving events form a short ice tongue. (b) Advected crevasses at the base of the glacier contribute to a second calving event extending the ice tongue. Tensile surface crevasses deepen upstream in response to adjusting stresses. (c) Advected tensile crevasses upstream cause another calving event with a small contribution from shear localization. This process continues leading to complete glacier collapse.

4.4.2 Submarine melt weakens ice to catastrophic retreat

Figure 4.6 shows that when submarine melt is included, the average calving front advance rate as a function of tensile strength and shear strength is largely unchanged. However, with submarine melt, the requisite initial retreat can be provided by mass loss due to melt rather than mass loss to incremental tensile calving events. This initial retreat is further accelerated by the chosen melt profile: a parabolic melt profile with maximum melt halfway between the water line and the bed produces glacier "feet" at the bed and aerial portions at the top of the calving front that are most susceptible to failure at lower yield strengths.

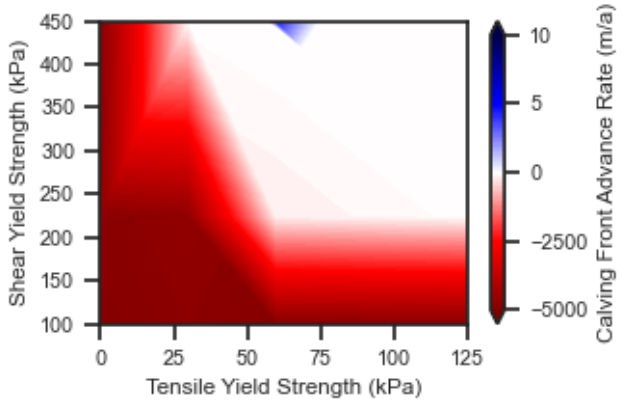

Figure 4.6: Average calving front advance rate over 10 years with varying tensile strengths and shear strengths for prograde bed with submarine melt. Calving behavior is less sensitive to varying the tensile strength, depending strongly on shear yield strength. Shear strengths greater than 225 kPa with a tensile strength greater than 60 kPa prevent catastrophic collapse through high material strength.

In addition, mass loss due to melt prevents slow glacier advance in the case of high tensile strength and high shear strength. Varying tensile strength at high shear strength again makes small adjustment to the average advance rate, but catastrophic collapse due to shear localization dominates behavior at lower shear strengths.

4.4.3 Pro-glacial sill stabilizes advance but not retreat

When a Gaussian sill is introduced to the bed geometry, at high yield strengths, overall glacier advance is stalled on the sill. This is consistent with results omitting shear localization and submarine melt (Chapter III). Figure 4.7 shows the region of catastrophic collapse appears similar to the case of the constant prograde bed without a sill, indicating that the sill does little to prevent the onset of marine ice cliff instability. It's primary effect remains limited to restricting glacier advance. Comparing Figure 4.6 and Figure 4.7 indicates that a shear strength of 225 approximately kPa is sufficient to prevent catastrophic collapse in both cases. Varying tensile strength at higher shear strengths again transitions between slow advance and retreat.

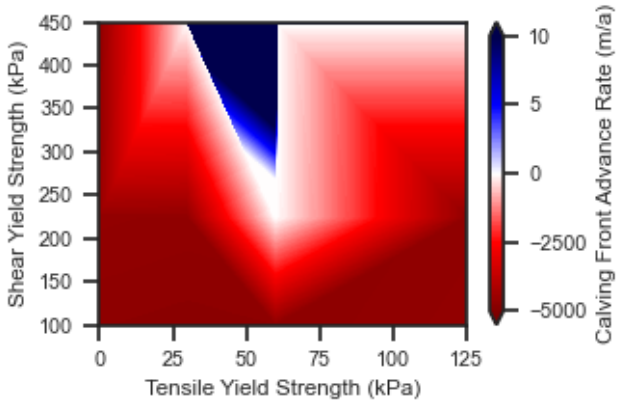

Figure 4.7: Average calving front advance rate over 10 years with varying tensile strengths and shear strengths for prograde bed with bump and submarine melt. Varying the tensile strength when shear strength is greater than 225 kPa changes advance rate. Shear strengths less than 225 kPa result in rapid retreat. This behavior is similar the test with a constant prograde bed, indicating that catastrophic collapse is not sensitive to a pro-glacial sill.

4.5 Discussion

In all of our tests, there is a portion of the failure envelope where the glacier reaches a marine ice cliff type instability and rapidly disintegrates. However, this behavior occurs primarily at shear strengths below 225 kPa. Using the linear elas-

tic fracture mechanics formulation to consistently specify both yield strengths, this would correspond to a tensile strength of 60 kPa.

Using our prescribed critical stress intensity factor and internal friction, a shear strength of 225 kPa gives a pre-existing starter flaw size of 0.2 m. These are relatively small strengths and large starter crack lengths compared to value ranges proposed by observation (Pfeffer, 1992) and used in previous modeling efforts (Moore and others, 2010), but not so large to be unrealistic for heavily damaged ice, as can be found near the terminus of outlet glaciers. Therefore, the fact that our model predicts a marine ice cliff instability in certain regimes, in spite of the lack of observations, points to a lack of stabilizing mechanisms.

Even if a marine ice cliff instability type collapse is initiated, it could be arrested by negative feedback mechanisms such as backstress from melange or piled up ice or stronger ice upstream that has undergone less melt and refreezing. However, this does not preclude the possibility of marine ice cliff instability in the past or in the future if glaciers retreat to high enough cliffs due to other forcings such as increased surface ablation, submarine melt, or hydrofracture.

Finally, the shear stress at a calving cliff scales linearly with cliff height (Bassis and Walker, 2012). As seen in Figure 4.5, glaciers considered in this study start with approximately 10 meters of freeboard in 150 meters of water, which is relatively small compared to large tidewater glaciers such as Thwaites glacier and Pine Island glacier in West Antarctica or larger Greenland glaciers such as Helheim or Jackobshavn. Thus, significantly higher shear strengths than 225 kPa are likely necessary to prevent catastrophic collapse for these large glaciers. For example, the grounding line of Thwaites glacier is currently approximately 600 meters below sea level. Using the estimate for the depth-averaged deviatoric stress as a function of cliff height and

water depth derived by Bassis and Walker (2012) and calculating using a hypothetical 50 meter cliff height for Thwaites glacier gives a factor of 10 increase in the shear strength necessary to prevent failure. This would bring estimates of pre-existing starter crack size into the range of a few millimeters, which is consistent with previous observations and models (Pfeffer, 1992; Moore and others, 2010).

4.6 Conclusion

Our study shows on idealized geometries that our full Stokes calving model including tensile crevasse advection, shear calving, and submarine melt can successfully reproduce glacier patterns of advance, steady state, slow retreat, and catastrophic retreat. Notably, in contrast to earlier work (Chapter III), the revised version of our model can produce sustained, gradual retreat and steady state behavior without a stabilizing sill.

Submarine melt lowers the net ice velocity by directly impacting the rate at which the calving front can advance. However, melt also has a demonstrable nonlinear effect on the net ice velocity by affecting calving rates. With the parabolic melt profile used in our study, melt is highest halfway between the bed and the water line. Over time, this causes an overhang to develop near the top of the calving front and a foot to develop at the base (for a grounding calving front). This calving front geometry is more susceptible to small calving events, hastening retreat and eventually triggering a marine ice cliff instability.

Regardless of the inclusion of submarine melt, our results show a high sensitivity of calving behavior to ice shear strength. Varying tensile strength provides small shifts to calving front advance rate in the absence of melt and when melt is included, the effect of varying tensile strength is largely eliminated. In contrast, all tests show

that catastrophic collapse is highly sensitive to shear strength. While lower shear strengths do not guarantee catastrophic collapse, avoiding a marine ice cliff stability at lower shear strengths appears highly sensitive to the exact glacier geometry and combination of other mass balance inputs to the system.

This work introduces a novel glacier flow and calving model that includes a variety of important mass balance mechanisms simultaneously, and future work would be well positioned to test this model on historical data to see how well observations can be matched and what tuning parameters including viscosity, yield strength, and submarine melt are most important to replicating observed behaviors.

CHAPTER V

Conclusion

Our work addresses the important consideration of crevasse advection on calving as well as the contribution of mixed mode failure in conjunction with the memory of previously crevassed ice. This is an effort towards better understanding the ice calving process, which accounts for a significant uncertainty in future sea level rise projections.

In Chapter II we showed the importance of carefully considering the ice-ocean boundary condition in full Stokes models that have a rapid calving mechanism. With the typical approximation used for full Stokes models in glaciology, adding a rapid calving mechanism can lead to stresses with an unphysical numerical origin. The simple re-addition of the acceleration term to the stress balance eliminates these numerical issues without noticeable computational cost. We implement this solution for all subsequent modeling efforts presented, and we hope that future calving studies using full Stokes models take note of this subtle numerical issue. For example, this solution has also been implemented in the newly developed m-ice model that considers different rheologies for different stress and strain regimes (Bassis and others, 2021).

Using numerical methods established in Chapter II, we proceed in Chapter III to

implement a full Stokes model with tensile calving and including crevasse advection using a particle-in-cell method. This extends upon previous work by adding crevasse advection to the established Nye's zero stress model, which is a popular implementation of calving. We test our model on idealized glacier geometries and show that adding crevasse advection to the Nye's zero stress model discourages ice tongue formation and can lead to temporary glacier retreat. Crevasse advection also enhances the stabilizing properties of a bump in the glacier bed. However, we do not observe catastrophic retreat in any cases, which is of high interest to the glaciological community due to the proposed "marine ice cliff instability". Our model's inability to produce catastrophic retreat motivates the inclusion of other mass loss mechanisms including submarine melt and mixed-mode failure. With simple idealized tests, we show in Chapter III that adding shear failure to our model would be sufficient to cause catastrophic retreat in some cases.

Improving on the crevasse advection model presented in Chapter III, we conclude in Chapter IV by including the shear localization process using a brittle compressive failure model and allow for calving to occur with fractures initiated through both shear and tensile failure. This model moves away from the Nye's zero criterion and allows for the tensile and compressive stress of ice to be defined consistently with material and microscopic properties of the glacier ice. In this updated model, we also add submarine melt as an additional source of mass loss. We test this improved model on the same idealized geometries in III and show that a sharp transition exists at critical yield strengths where the glacier transitions from steady state behavior to catastrophic collapse. Adding submarine melt increases overall mass loss, but does not alter the threshold shear strength necessary to avoid rapid collapse. In reality, this collapse could be mitigated by negative feedbacks such as backstress

from mélange buildup due to calving.

Based on the model development presented here, future work would be well motivated to implement mélange backstress, given that mélange formation after calving provides some stabilization to future calving until ice has been removed from proximity to the calving front. Additionally, model results on observational data of Greenland or Antarctic glaciers would provide insight on the most important parameters to replicate observed glacier advance and retreat patterns. However, in addition to parameters such as ice fracture toughness and pre-existing crack sizes that directly impact the calving model, considerations such as ice rheology and basal sliding law can significantly alter model results and are not direct inputs to the calving model. The importance of rheology and basal sliding is apparent in Chapter III, where we see significantly different calving results based on changing ice temperature and sliding coefficient. Thus, model studies of observational data must take care to explore the full parameter space and not simply the space directly related to the calving law.

Bibliography

Alnæs M, Blechta J, Hake J, Johansson A, Kehlet B, Logg A, Richardson C, Ring J, Rognes ME and Wells GN (2015) The fenics project version 1.5. *Archive of Numerical Software*, **3**(100), 9–23 (doi: 10.11588/ans.2015.100.20553)

Altizer S, Ostfeld RS, Johnson PTJ, Kutz S and Harvell CD (2013) Climate change and infectious diseases: From evidence to a predictive framework. *Science*, **341**(6145), 514–519 (doi: 10.1126/science.1239401)

Ashby M and Hallam (Née Cooksley) S (1986) The failure of brittle solids containing small cracks under compressive stress states. *Acta Metallurgica*, **34**(3), 497–510 (doi: 10.1016/0001-6160(86)90086-6)

Barnard PL, Erikson LH, Foxgrover AC, Hart JAF, Limber P, O'Neill AC, van Ormondt M, Vitousek S, Wood N, Hayden MK and others (2019) Dynamic flood modeling essential to assess the coastal impacts of climate change. *Scientific reports*, **9**(1), 1–13 (doi: 10.1038/s41598-019-40742-z)

Barnett J, Graham S, Mortreux C, Fincher R, Waters E and Hurlimann A (2014) A local coastal adaptation pathway. *Nature Climate Change*, **4**(12), 1103–1108 (doi: 10.1038/nclimate2383)

Bassis JN and Walker CC (2012) Upper and lower limits on the stability of calving glaciers from the yield strength envelope of ice. *Proceedings of the Royal Society*

A: Mathematical, Physical and Engineering Sciences, **468**(2140), 913–931 (doi: 10.1098/rspa.2011.0422)

Bassis JN, Petersen SV and Mac Cathles L (2017) Heinrich events triggered by ocean forcing and modulated by isostatic adjustment. *Nature*, **542**(7641), 332–334 (doi: 10.1038/nature21069)

Bassis JN, Berg B, Crawford AJ and Benn DI (2021) Transition to marine ice cliff instability controlled by ice thickness gradients and velocity. *Science*, **372**(6548), 1342–1344 (doi: 10.1126/science.abf6271)

Bellprat O, Guemas V, Doblas-Reyes F and Donat MG (2019) Towards reliable extreme weather and climate event attribution. *Nature communications*, **10**(1), 1–7 (doi: 10.1038/s41467-019-09729-2)

Benn DI, Åström J, Zwinger T, Todd J, Nick FM, Cook S, Hulton NR and Luckman A (2017) Melt-under-cutting and buoyancy-driven calving from tidewater glaciers: new insights from discrete element and continuum model simulations. *J. Glaciol.*, **63**, 691–702 (doi: 10.1017/jog.2017.41)

Berg B and Bassis J (2020) Brief communication: Time step dependence (and fixes) in stokes simulations of calving ice shelves. *The Cryosphere*, **14**, 3209–3213 (doi: 10.5194/tc-14-3209-2020)

Borstad CP, Khazendar A, Larour E, Morlighem M, Rignot E, Schodlok MP and Seroussi H (2012) A damage mechanics assessment of the larsen b ice shelf prior to collapse: Toward a physically-based calving law. *Geophysical Research Letters*, **39**(18) (doi: 10.1029/2012GL053317)

Bowles L (1996) *Foundation analysis and design*. McGraw-hill

Chen J and Mueller V (2018) Coastal climate change, soil salinity and human migration in bangladesh. *Nature Climate Change*, **8**(11), 981–985 (doi: 10.1038/s41558-018-0313-8)

Choi Y, Morlighem M, Wood M and Bondzio JH (2018) Comparison of four calving laws to model greenland outlet glaciers. *The Cryosphere*, **12** (doi: 10.5194/tc-12-3735-2018)

Clerc F, Minchew BM and Behn MD (2019) Marine ice cliff instability mitigated by slow removal of ice shelves. *Geophysical Research Letters*, **46**(21), 12108–12116 (doi: 10.1029/2019GL084183)

Crawford AJ, Benn DI, Todd J, Åström JA, Bassis JN and Zwinger T (2021) Marine ice-cliff instability modeling shows mixed-mode ice-cliff failure and yields calving rate parameterization. *Nature Communications*, **12**(1), 1–9 (doi: 10.1038/s41467-021-23070-7)

Cuffey KM and Paterson WSB (2010) *The physics of glaciers*. Elsevier, Butterworth-Heineman, Burlington, MA, 4 edition

Dasgupta S, Laplante B, Meisner C, Wheeler D and Yan J (2009) The impact of sea level rise on developing countries: a comparative analysis. *Climatic change*, **93**(3), 379–388 (doi: 10.1007/s10584-008-9499-5)

De Andrés E, Otero J, Navarro F, Promińska A, Lapazaran J and Walczowski W (2018) A two-dimensional glacier–fjord coupled model applied to estimate submarine melt rates and front position changes of hansbreen, svalbard. *Journal of Glaciology*, **64**(247), 745–758 (doi: 10.1017/jog.2018.61)

DeConto RM, Pollard D, Alley RB, Velicogna I, Gasson E, Gomez N, Sadai S,

Condron A, Gilford DM, Ashe EL and others (2021) The paris climate agreement and future sea-level rise from antarctica. *Nature*, **593**(7857), 83–89 (doi: 10.1038/s41586-021-03427-0)

Depoorter MA, Bamber JL, Griggs JA, Lenaerts JT, Ligtenberg SR, van den Broeke MR and Moholdt G (2013) Calving fluxes and basal melt rates of antarctic ice shelves. *Nature*, **502**(7469), 89–92 (doi: 10.1038/nature12567)

Duddu R, Bassis JN and Waisman H (2013) A numerical investigation of surface crevasse propagation in glaciers using nonlocal continuum damage mechanics. *Geophysical Research Letters*, **40**(12), 3064–3068 (doi: 10.1002/grl.50602)

Dunse T, Schuler T, Hagen J and Reijmer C (2012) Seasonal speed-up of two outlet glaciers of austfonna, svalbard, inferred from continuous gps measurements. *The Cryosphere*, **6**, 453–466 (doi: 10.5194/tc-6-453-2012)

Durand G, Gagliardini O, De Fleurian B, Zwinger T and Le Meur E (2009) Marine ice sheet dynamics: Hysteresis and neutral equilibrium. *Journal of Geophysical Research: Earth Surface*, **114**(F3) (doi: 10.1029/2008JF001170)

Duval P, Montagnat M, Grennerat F, Weiss J, Meyssonnier J and Philip A (2010) Creep and plasticity of glacier ice: a material science perspective. *Journal of Glaciology*, **56**(200), 1059–1068 (doi: 10.3189/002214311796406185)

Edwards TL, Nowicki S, Marzeion B, Hock R, Goelzer H, Seroussi H, Jourdain NC, Slater DA, Turner FE, Smith CJ and others (2021) Projected land ice contributions to twenty-first-century sea level rise. *Nature*, **593**(7857), 74–82 (doi: 10.1038/s41586-021-03302-y)

Enderlin EM and Bartholomaus TC (2020) Sharp contrasts in observed and mod-

eled crevasse patterns at greenland's marine terminating glaciers. *The Cryosphere*, **14**(11), 4121–4133 (doi: 10.5194/tc-14-4121-2020)

Enderlin EM and Howat IM (2013) Submarine melt rate estimates for floating termini of greenland outlet glaciers (2000–2010). *Journal of Glaciology*, **59**(213), 67–75 (doi: 10.3189/2013JoG12J049)

Gagliardini O, Zwinger T, Gillet-Chaulet F, Durand G, Favier L, de Fleurian B, Greve R, Malinen M, Martín C, Råback P, Ruokolainen J, Sacchettini M, Schäfer M, Seddik H and Thies J (2013) Capabilities and performance of elmer/ice, a new-generation ice sheet model. *Geosci. Model. Dev.*, **6**, 1299–1318 (doi: 10.5194/gmd-6-1299-2013)

Geuzaine C and Remacle JF (2009) Gmsh: A 3-d finite element mesh generator with built-in pre-and post-processing facilities. *International journal for numerical methods in engineering*, **79**(11), 1309–1331 (doi: 10.1002/nme.2579)

Greve R and Blatter H (2009) *Dynamics of ice sheets and glaciers*. Springer, Berlin

Haasnoot M, Kwadijk J, Van Alphen J, Le Bars D, Van Den Hurk B, Diermanse F, Van Der Spek A, Essink GO, Delsman J and Mens M (2020) Adaptation to uncertain sea-level rise; how uncertainty in antarctic mass-loss impacts the coastal adaptation strategy of the netherlands. *Environmental Research Letters*, **15**(3), 034007 (doi: 10.1088/1748-9326/ab666c)

Harrington JA, Humphrey NF and Harper JT (2015) Temperature distribution and thermal anomalies along a flowline of the greenland ice sheet. *Annals of Glaciology*, **56**(70), 98–104 (doi: 10.3189/2015AoG70A945)

Hauer ME, Evans JM and Mishra DR (2016) Millions projected to be at risk from

sea-level rise in the continental united states. *Nature Climate Change*, **6**(7), 691–695 (doi: 10.1038/nclimate2961)

Helanow C and Ahlkrona J (2018) Stabilized equal low-order finite elements in ice sheet modeling – accuracy and robustness. *Computational Geosciences*, **22**(4), 951–974, ISSN 1573-1499 (doi: 10.1007/s10596-017-9713-5)

Hooke R (2005) *The Principles of Glacier Mechanics*. Cambridge University Press

Howat IM, Box JE, Ahn Y, Herrington A and McFadden EM (2010) Seasonal variability in the dynamics of marine-terminating outlet glaciers in greenland. *Journal of Glaciology*, **56**(198), 601–613 (doi: 10.3189/002214310793146232)

Iken A, Echelmeyer K, Harrison W and Funk M (1993) Mechanisms of fast flow in jakobshavns isbræ, west greenland: Part i. measurements of temperature and water level in deep boreholes. *Journal of Glaciology*, **39**(131), 15–25 (doi: 10.3189/S0022143000015689)

Jaeger JC, Cook NG and Zimmerman R (2009) *Fundamentals of rock mechanics*. John Wiley & Sons

Jiménez S and Duddu R (2018) On the evaluation of the stress intensity factor in calving models using linear elastic fracture mechanics. *Journal of Glaciology*, **64**(247), 759–770 (doi: 10.1017/jog.2018.64)

Jiménez S, Duddu R and Bassis J (2017) An updated-lagrangian damage mechanics formulation for modeling the creeping flow and fracture of ice sheets. *Computer Methods in Applied Mechanics and Engineering*, **313**, 406–432 (doi: 10.1016/j.cma.2016.09.034)

Joughin I, Smith BE, Howat IM, Floricioiu D, Alley RB, Truffer M and Fahnestock M (2012) Seasonal to decadal scale variations in the surface velocity of jakobshavn isbrae, greenland: Observation and model-based analysis. *Journal of Geophysical Research: Earth Surface*, **117**(F2) (doi: 10.1029/2011JF002110)

Kennedy F, Schulson E and Jones D (2000) The friction of ice on ice at low sliding velocities. *Philosophical Magazine A*, **80**(5), 1093–1110 (doi: 10.1080/01418610008212103)

Khan SA, Aschwanden A, Bjørk AA, Wahr J, Kjeldsen KK and Kjær KH (2015) Greenland ice sheet mass balance: a review. *Reports on Progress in Physics*, **78**(4), 046801 (doi: 10.1088/0034-4885/78/4/046801)

Krug J, Weiss J, Gagliardini O and Durand G (2014) Combining damage and fracture mechanics to model calving. *The Cryosphere*, **8**, 2101–2117 (doi: 10.5194/tc-8-2101-2014)

Lafferty KD (2009) The ecology of climate change and infectious diseases. *Ecology*, **90**(4), 888–900 (doi: 10.1890/08-0079.1)

Levermann A, Albrecht T, Winkelmann R, Martin MA, Haseloff M and Joughin I (2012) Kinematic first-order calving law implies potential for abrupt ice-shelf retreat. *The Cryosphere*, **6**, 273–286 (doi: 10.5194/tc-6-273-2012)

Luckman A, Benn DI, Cottier F, Bevan S, Nilsen F and Inall M (2015) Calving rates at tidewater glaciers vary strongly with ocean temperature. *Nature communications*, **6**(1), 1–7 (doi: 10.1038/ncomms9566)

Lüthi M, Funk M, Iken A, Gogineni S and Truffer M (2002) Mechanisms of fast flow in jakobshavn isbræ, west greenland: Part iii. measurements of ice deformation,

temperature and cross-borehole conductivity in boreholes to the bedrock. *Journal of Glaciology*, **48**(162), 369–385 (doi: 10.3189/172756502781831322)

Ma Y and Bassis JN (2019) The effect of submarine melting on calving from marine terminating glaciers. *Journal of Geophysical Research: Earth Surface*, **124**(2), 334–346 (doi: 10.1029/2018JF004820)

Ma Y, Tripathy CS and Bassis JN (2017) Bounds on the calving cliff height of marine terminating glaciers. *Geophysical Research Letters*, **44**(3), 1369–1375 (doi: 10.1002/2016GL071560)

Maljaars JM, Richardson CN and Sime N (2020) Leopart: a particle library for fenics. *Computers & Mathematics with Applications* (doi: 10.1016/j.camwa.2020.04.023)

Moore FC, Baldos U, Hertel T and Diaz D (2017) New science of climate change impacts on agriculture implies higher social cost of carbon. *Nature communications*, **8**(1), 1–9 (doi: 10.1038/s41467-017-01792-x)

Moore PL, Iverson NR and Cohen D (2010) Conditions for thrust faulting in a glacier. *Journal of Geophysical Research: Earth Surface*, **115**(F2) (doi: 10.1029/2009JF001307)

Morlighem M, Bondzio J, Seroussi H, Rignot E, Larour E, Humbert A and Rebuffi S (2016) Modeling of store gletscher's calving dynamics, west greenland, in response to ocean thermal forcing. *Geophysical Research Letters*, **43**(6), 2659–2666 (doi: 10.1002/2016GL067695)

Mottram RH and Benn DI (2009) Testing crevasse-depth models: a field study at breiðamerkurjökull, iceland. *Journal of Glaciology*, **55**(192), 746–752 (doi: 10.3189/002214309789470905)

Mouginot J, Scheuchl B and Rignot E (2012) Mapping of ice motion in antarctica using synthetic-aperture radar data. *Remote Sens-Basel*, **4**, 2753–2767 (doi: 10.3390/rs4092753)

Nick FM, Van der Veen CJ, Vieli A and Benn DI (2010) A physically based calving model applied to marine outlet glaciers and implications for the glacier dynamics. *Journal of Glaciology*, **56**(199), 781–794 (doi: 10.3189/002214310794457344)

Nye JF (1957) The distribution of stress and velocity in glaciers and ice-sheets. *Proceedings of the Royal Society of London. Series A. Mathematical and Physical Sciences*, **239**(1216), 113–133 (doi: 10.1098/rspa.1957.0026)

Østby TI, Schuler TV, Hagen JO, Hock R and Reijmer CH (2013) Parameter uncertainty, refreezing and surface energy balance modelling at austfonna ice cap, svalbard, 2004-08. *Annals of glaciology*, **54**(63), 229–240 (doi: 10.3189/2013AoG63A280)

Paden J, Li J, Leuschen C, Rodriguez-Morales F and Hale R (2010, updated 2018) Icebridge mcords l2 ice thickness, version 1. *Boulder, Colorado USA. NASA National Snow and Ice Data Center Distributed Active Archive Center* (doi: 10.5067/GDQ0CUCVTE2Q)

Pattyn F and Morlighem M (2020) The uncertain future of the antarctic ice sheet. *Science*, **367**(6484), 1331–1335 (doi: 10.1126/science.aaz5487)

Pattyn F, Schoof C, Perichon L, Hindmarsh R, Bueler E, De Fleurian B, Durand G, Gagliardini O, Gladstone R, Goldberg D and others (2012) Results of the marine ice sheet model intercomparison project, mismip. *The Cryosphere*, **6**(3), 573–588 (doi: 10.5194/tc-6-573-2012)

Pfeffer WT (1992) Stress-induced foliation in the terminus of variegated glacier, alaska, usa, formed during the 1982–83 surge. *Journal of Glaciology*, **38**(129), 213–222 (doi: 10.3189/S0022143000003622)

Pörtner HO, Roberts D, Masson-Delmotte V, Zhai P, Tignor M, Poloczanska E, Mintenback K, Alegría A, Nicolai M, Okem A, Petzold J, Rama B, Weyer N and others (2019) Ipcc special report on the ocean and cryosphere in a changing climate. *In press*

Pralong A and Funk M (2005) Dynamic damage model of crevasse opening and application to glacier calving. *Journal of Geophysical Research: Solid Earth*, **110**(B1) (doi: 10.1029/2004JB003104)

Renshaw C and Schulson E (2001) Universal behaviour in compressive failure of brittle materials. *Nature*, **412**, 897–900 (doi: 10.1038/35091045)

Rignot E, Mouginot J and Scheuchl B (2011) Ice flow of the antarctic ice sheet. *Science*, **333**, 1427–1430 (doi: 10.1126/science.1208336)

Rignot E, Fenty I, Xu Y, Cai C and Kemp C (2015) Undercutting of marine-terminating glaciers in west greenland. *Geophysical Research Letters*, **42**(14), 5909–5917 (doi: 10.1002/2015GL064236)

Rignot E, Mouginot J and Scheuchl B (2017) Measures insar-based antarctica ice velocity map, version 2. *Boulder, Colorado USA. NASA National Snow and Ice Data Center Distributed Active Archive Center* (doi: 10.5067/D7GK8F5J8M8R)

Schuler TV, Loe E, Taurisano A, Eiken T, Hagen JO and Kohler J (2007) Calibrating a surface mass-balance model for austfonna ice cap, svalbard. *Annals of Glaciology*, **46**, 241–248 (doi: 10.3189/172756407782871783)

Schulson E (2002) Compressive shear faults in ice: plastic vs. coulombic faults. *Acta Materialia*, **50**(13), 3415–3424, ISSN 1359-6454 (doi: 10.1016/S1359-6454(02)00154-4)

Schulson EM (2001) Brittle failure of ice. *Engineering Fracture Mechanics*, **68**(17), 1839–1887 (doi: 10.1016/S0013-7944(01)00037-6)

Sciascia R, Straneo F, Cenedese C and Heimbach P (2013) Seasonal variability of submarine melt rate and circulation in an east greenland fjord. *Journal of Geophysical Research: Oceans*, **118**(5), 2492–2506 (doi: 10.1002/jgrc.20142)

Slater DA, Nienow P, Goldberg D, Cowton T and Sole A (2017) A model for tidewater glacier undercutting by submarine melting. *Geophysical Research Letters*, **44**(5), 2360–2368 (doi: 10.1002/2016GL072374)

Stocker TF, Qin D, Plattner GK, Tignor M, Allen SK, Boschung J, Nauels A, Xia Y, Bex V, Midgley PM and others (2013) Climate change 2013: The physical science basis. *Contribution of working group I to the fifth assessment report of the intergovernmental panel on climate change*, **1535**

Todd J and Christoffersen P (2014) Are seasonal calving dynamics forced by buttressing from ice mélange or undercutting by melting? outcomes from full-stokes simulations of store gletscher, west greenland. *The Cryosphere*, **8**, 2353–2365 (doi: 10.5194/tc-8-2353-2014)

Todd J, Christoffersen P, Zwinger T, Råback P, Chauché N, Benn D, Luckman A, Ryan J, Toberg N, Slater D and Hubbard A (2018) A full-stokes 3-d calving model applied to a large greenlandic glacier. *J. Geophys. Res-Earth.*, **123**, 410–432 (doi: 10.1002/2017JF004349)

Todd J, Christoffersen P, Zwinger T, Råback P and Benn DI (2019) Sensitivity of a calving glacier to ice–ocean interactions under climate change: new insights from a 3-d full-stokes model. *The Cryosphere*, **13**(6), 1681–1694 (doi: 10.5194/tc-13-1681-2019)

Truffer M and Motyka RJ (2016) Where glaciers meet water: Subaqueous melt and its relevance to glaciers in various settings. *Reviews of Geophysics*, **54**(1), 220–239 (doi: 10.1002/2015RG000494)

Tsai VC and Rice JR (2010) A model for turbulent hydraulic fracture and application to crack propagation at glacier beds. *Journal of Geophysical Research: Earth Surface*, **115**(F3) (doi: 10.1029/2009JF001474)

van den Broeke M, Bamber J, Ettema J, Rignot E, Schrama E, van de Berg WJ, van Meijgaard E, Velicogna I and Wouters B (2009) Partitioning recent greenland mass loss. *science*, **326**(5955), 984–986 (doi: 10.1126/science.1178176)

Vieli A, Funk M and Blatter H (2001) Flow dynamics of tidewater glaciers: a numerical modelling approach. *Journal of Glaciology*, **47**(159), 595–606 (doi: 10.3189/172756501781831747)

Wagner TJW, Wadhams P, Bates R, Elosegui P, Stern A, Vella D, Abrahamsen EP, Crawford A and Nicholls KW (2014) The "footloose" mechanism: Iceberg decay from hydrostatic stresses. *Geophys. Res. Lett.*, **41**, 5522–5529 (doi: 10.1002/2014GL060832)

Walter F, Chaput J and Lüthi MP (2014) Thick sediments beneath greenland's ablation zone and their potential role in future ice sheet dynamics. *Geology*, **42**(6), 487–490 (doi: 10.1130/G35492.1)

Wise MG, Dowdeswell JA, Jakobsson M and Larter RD (2017) Evidence of marine ice-cliff instability in pine island bay from iceberg-keel plough marks. *Nature*, **550**(7677), 506–510 (doi: 10.1038/nature24458)

Yu H, Rignot E, Morlighem M and Seroussi H (2017) Iceberg calving of thwaites glacier, west antarctica: full-stokes modeling combined with linear elastic fracture mechanics. *The Cryosphere*, **11**, 1283 (doi: 10.5194/tc-11-1283-2017)

Zanocco C, Boudet H, Nilson R, Satein H, Whitley H and Flora J (2018) Place, proximity, and perceived harm: extreme weather events and views about climate change. *Climatic Change*, **149**(3), 349–365 (doi: 10.1007/s10584-018-2251-x)